Monthly Notices of the ROYAL ASTRONOMICAL SOCIETY

MNRAS **500,** 5024–5042 (2021) doi:10.1093/mnras/staa3080
Advance Access publication 2020 October 20

Subaru/HSC deep optical imaging of infrared sources in the AKARI North Ecliptic Pole-Wide field

Nagisa Oi [1,2]★ Tomotsugu Goto,[3] Hideo Matsuhara,[4,5] Yousuke Utsumi,[6,7,8] Rieko Momose,[3,9] Yoshoki Toba [10,11,12] Matthew Malkan,[13] Toshinobu Takagi,[14] Ting-Chi Huang [4] Seong Jin Kim [3] and Youichi Ohyama[10]

[1]*Faculty of Science Division II, Liberal Arts, Tokyo University of Science, 1-3, Kagurazaka, Shinjuku-ku, Tokyo 162-8601, Japan*
[2]*School of Science and Technology, Kwansei Gakuin University, Gakuen, Sanda, Hyogo 669-1337, Japan*
[3]*Institute of Astronomy, National Tsing Hua University, No. 101, Section 2, Kuang-Fu Road, Hsinchu 30013, Taiwan*
[4]*Institute of Space and Astronautical Science, Japan Aerospace Exploration Agency, 3-1-1 Yoshinodai, Chuo-ku, Sagamihara, Kanagawa 252-5210, Japan*
[5]*Department of Space and Astronautical Science, Graduate University for Advanced Studies, SOKENDAI, Shonankokusaimura, Hayama, Miura District, Kanagawa 240-0193, Japan*
[6]*SLAC National Accelerator Laboratory, 2575 Sand Hill Road, Menlo Park, CA 94025, USA*
[7]*Kavli Institute for Particle Astrophysics and Cosmology, Stanford University, 452 Lomita Mall, Stanford, CA 94035, USA*
[8]*Hiroshima Astrophysical Science Center, Hiroshima University, 1-3-1 Kagamiyama, Higashi-Hiroshima, Hiroshima 739-8526, Japan*
[9]*Department of Astronomy, School of Science, The University of Tokyo, 7-3-1 Hongo, Bunkyo-ku, Tokyo 113-0033, Japan*
[10]*Academia Sinica Institute of Astronomy and Astrophysics, 11F of Astronomy-Mathematics Building, AS/NTU, No. 1, Section 4, Roosevelt Road, Taipei 10617, Taiwan*
[11]*Department of Astronomy, Kyoto University, Kitashirakawa-Oiwake-cho, Sakyo-ku, Kyoto 606-8502, Japan*
[12]*Research Center for Space and Cosmic Evolution, Ehime University, 2-5 Bunkyo-cho, Matsuyama, Ehime 790-8577, Japan*
[13]*Department of Physics and Astronomy, UCLA, Los Angeles, CA 90095-1547, USA*
[14]*Japan Space Forum, Shin-Ochanomizu Urban Trinity Bldg. 2F, 3-2-1, Kandasurugadai, Chiyoda-ku, Tokyo 101-0062, Japan*

Accepted 2020 September 29. Received 2020 September 7; in original form 2020 February 6

ABSTRACT

We present a five-broad-band (*grizy*) photometric catalogue of Subaru/Hyper Suprime-Cam (HSC) optical imaging observations at around the North Ecliptic Pole (NEP) where the AKARI infrared (IR) satellite conducted a large survey (NEP-Wide survey). The observations cover almost all the NEP-Wide survey field down to the depth of 28.1, 26.8, 26.3, 25.5, and 25.0 mag (5σ) at *grizy*, respectively. The five-band HSC catalogue contains about 2.6 million objects, and 70 959 AKARI NEP-Wide counterpart sources are identified in the catalogue. We added existing supplementary catalogues from the *u* band to the far-IR band, and estimated photo-*z* for the AKARI-HSC sources. We achieved $\sigma_{\Delta z/(1+zs)} = 0.06$ and an outlier rate of 13.4 per cent at $z = 0.2$–1.5. Using the spectral energy distribution (SED) template fitting, we classified the AKARI-HSC galaxies into four categories, namely quiescent, star-forming, Type1 active galactic nucleus (AGN), and Type2 AGN, in each redshift bin. At $z > 1$, the mean SED of star-forming galaxies in mid-IR (3–10 μm) range is significantly different from that of spiral galaxies in the nearby Universe, indicating that many of star-forming galaxies at $z > 1$ contain a heat source capable of heating dust to temperatures that radiate thermal emission in the mid-IR range. Furthermore, we estimated the number fraction of AGNs ($f_{\rm AGN}$) in each bin of redshift and IR luminosity ($L_{\rm IR}$), and examined the dependence of redshift and $L_{\rm IR}$. In $\log(L_{\rm IR}/{\rm L}_\odot) = 11.0$–14.0, the $f_{\rm AGN}$ shows a significant increase with increasing redshift, regardless of the $L_{\rm IR}$ bins. In contrast, the $f_{\rm AGN}$ shows a slight increase against $L_{\rm IR}$ at $z < 1$ and no increase with increasing $L_{\rm IR}$ at $z > 1$.

Key words: galaxies: evolution – galaxies: photometry – galaxies: starburst – galaxies: star formation – infrared: galaxies.

1 INTRODUCTION

Luminous infrared galaxies (LIRGs; infrared luminosity $L_{\rm IR} = 10^{11}$–$10^{12}\,{\rm L}_\odot$) and ultra-luminous galaxies (ULIRGs; $L_{\rm IR} = 10^{12}$–$10^{13}\,{\rm L}_\odot$) are playing an important role in the galaxy formation and evolution. In the local Universe, a large fraction of these galaxies are interacting system (> 60 per cent for LIRGs and > 90 per cent for ULIRGs; Murphy et al. 1996; Sanders & Mirabel 1996), indicating that these galaxies are in an active and critical phase on their evolution. The bulk of the energy hidden by dust is generated by stars and/or released by mass accretion on to a supermassive black hole, i.e. active galactic nucleus (AGN) activity. At least 25 per cent–30 per cent of ULIRGs show signs of the AGN activity (Kim, Veilleux & Sanders 1998; Goto et al. 2011), and it increases with luminosity to 35 per cent–50 per cent. Studies of the extragalactic background have suggested that at least one-third of the luminous energy generated by stars has been hidden and reprocessed

★ E-mail: nagisaoi@rs.tus.ac.jp

into the infrared (IR) by dust (Puget et al. 1996; Lagache et al. 1999; Stecker, Malkan & Scully 2006; Franceschini, Rodighiero & Vaccari 2008), and the contribution of IR luminous sources to the cosmic IR luminosity density increases with redshift, dominated by LIRGs at $z > 0.7$ (Le Floc'h et al. 2005) and by ULIRGs at $z \sim 2$ (Caputi et al. 2007).

After a Japanese IR space telescope, AKARI (Murakami et al. 2007), was launched in 2006 February, many studies of IR galaxies' properties have been performed. The AKARI satellite carried out a large-area survey in the direction of the North Ecliptic Pole (NEP), the so-called NEP survey (Matsuhara et al. 2006). The NEP survey is composed of two parts: a wide survey (NEP-Wide; 5.4 sq. deg; Lee et al. 2009; Kim et al. 2012) and a deep survey (NEP-Deep; 0.6 sq. deg; Wada et al. 2008; Takagi et al. 2012; Murata et al. 2013) with nine filters (*N*2, *N*3, *N*4, *S*7, *S*9*W*, *S*11, *L*15, *L*18*W*, and *L*24) of the Infrared Camera (IRC; Onaka et al. 2007). The reference wavelengths of the nine filters are 2.4, 3.2, 4.1, 7.0, 9.0, 11.0, 15.0, 18.0, and 24.0 μm, respectively. The filters cover the entire wavelength range from 2 to 24 μm continuously, and critically include the gap between *Spitzer* Infrared Array Camera (IRAC; Fazio et al. 2004) and Multiband Imaging Photometer (MIPS; Rieke et al. 2004) instruments from 8 to 24 μm where only the peak-up imagers on the *Spitzer* Infrared Spectrograph (Houck et al. 2004) instrument are available with the small field of view (FoV; 0.9 arcmin × 1.3 arcmin). This continuous wavelength coverage gives us the advantage of finding a sign of AGN activity because the shapes of spectral energy distributions (SEDs) of stellar component and AGN component show clear difference at ∼3–15 μm due to the difference of dust temperature heated by stars and by AGN. Indeed, many studies have been conducted on properties of stellar and AGN components of IR galaxies and its evolution from various aspects using the NEP survey data, i.e. luminosity function evolution of IR galaxies at $z < 1.5$ (Goto et al. 2010, 2015), luminosity function of mid-IR galaxies for low-z ($z < 0.3$; Kim et al. 2015), star formation and AGN activities at $z = 0.4$–2.0 (Hanami et al. 2012), relation of star formation and AGN at $z < 2$ (Karouzos et al. 2014), polycyclic aromatic hydrocarbon (PAH) feature deficit at $z < 2$ (Murata et al. 2014) and PAH deficit phenomena in the local ($z < 0.9$) Universe (Kim et al. 2019), dust attenuation at $z < 2$ (Buat et al. 2015), metallicity at $z \sim 0.9$ (Oi et al. 2017), and AGN fraction at $z < 3$ (Huang et al. 2017), along with multiwavelength data set from X-ray to radio, i.e. *Chandra* (Krumpe et al. 2015), the Galaxy Evolution Explorer (GALEX) Programme GI4-057001-AKARI-NEP, P.I. M. Malkan, Subaru (Wada et al. 2008), the Canada-France-Hawaii Telescope (CFHT) (Oi et al. 2014), *Herschel* (Pearson et al. 2014, 2017; Burgarella et al. 2019), the James Clerk Maxwell Telescope (JCMT) (Geach et al. 2017), and the Westerbork Synthesis Radio Telescope (WSRT) (White et al. 2010).

However, those researches on the properties of IR galaxies were limited by poor optical coverage both in area and depth in the AKARI NEP field. Over the NEP-Wide area, only shallow optical–near-IR imaging data are available (Hwang et al. 2007; Jeon et al. 2010), and intermediate-depth optical data ($r \sim 25.9$ AB mag; Oi et al. 2014) cover only 1 sq. deg over the NEP-Deep survey field, and deep optical data ($B \sim 28$ AB mag) are limited at a central 0.25 sq. deg. Since it is difficult to estimate the photometric redshift of optically faint IR galaxies using shallow optical data, redshift estimates have been performed only for objects in the NEP-Deep region (Oi et al. 2014) and for a limited subset of galaxies within the NEP-Wide region (Karouzos et al. 2014). Thus, various evolutionary studies, such as the number density of IR sources or the evolution of AGN existence rates in IR galaxies, were suffering because of the lack of redshift information. In order to study the evolution of IR sources in the NEP-Wide region using the unique IR data set with multiband data from X-rays to radio wavelength, deep optical data covering over the wide area are essential.

In this paper, we present a new deep optical imaging observation covering almost all the NEP-Wide survey area with Subaru/Hyper Suprime-Cam (HSC; Miyazaki et al. 2012, 2018). We also combined other existing wavelength data sets from the u^* band to the far-IR 500 μm to build wide-wavelength SEDs for the AKARI NEP-Wide IR sources, and estimated the photometric redshifts using the publicly available LE PHARE code. This paper is composed as follows: We describe our HSC observations and data reduction in Section 2. We cross-match of our HSC catalogue with the AKARI NEP-Wide catalogue and add other band catalogues in Section 3. Photometric redshift calculation with the multiband data set using SED fitting is in Section 4. By performing SED fitting using a local galaxy model template, we classified AKARI-HSC objects by four galaxy categories and discussed the SED shape evolution and the AGN number ratio evolution for IR galaxies in Section 5. Then, we summarize our results in the final section. We adopt $\Omega_m = 0.27$, $\Omega_\lambda = 0.73$, and $H_0 = 70$ km s^{-1} Mpc^{-1}.

2 HSC OBSERVATION AT NEP

2.1 HSC observation and data reduction

The Subaru/HSC provides a 1.5 deg in diameter FoV covered with 104 red-sensitive CCDs with the pixel scale of 0.17 arcsec. It has the largest FoV among optical cameras on an 8 m telescope and can cover almost all the AKARI NEP-Wide field that is 5.4 sq. deg with only four FoVs.

Our Subaru/HSC observations were carried out around the NEP (Fig. 1) in one night (June 30) in 2014 and four nights (August 7–10) in 2015. We could use only the *r*-band filter in 2014 because instrumental trouble occurred and the filter exchanger unit could not work. Then we observed around the NEP with seven FoVs to cover the whole NEP-Wide field in *r* band (pink circles in the left-hand panel of Fig. 1). In the S15B run, we took imaging data with the rest of four broad-band filters (*g*, *i*, *z*, and *y*) with four FoVs (blue circles). The total exposure time for each filter is summarized in Table 1. We executed the data reductions, including processes of bias and dark subtractions, flat-fielding of raw images, mosaicking, and stacking to create coadd images, building single-band catalogues, and merging the catalogues to create a multiband catalogue, using an HSC data analysis pipeline (Bosch et al. 2018) version 4.0.1 (hereafter `hscPipe`), which supports the HSC data of the S15B semester. We followed the standard reduction processes. The astrometric and photometric calibrations are performed relative to the Pan-STARRS1 (PS1; Schlafly et al. 2012; Tonry et al. 2012; Magnier et al. 2013; Chambers et al. 2016) survey data.[1]

The `hscPipe` creates a 'tract' that is each region of the sky cut into blocks, and then makes a mosaic for each tract. In the regular reduction process of the HSC data for a small sky area such as a 1 FoV with dithering, defining a special tract including all the HSC data is recommended. However, our HSC data are spread out over ∼5.4 sq. deg with the four or seven FoVs. Hence, we decided to use tracts defined by the HSC-SSP team, which is cut from the sky simply offhand. A tract is also separated into small patches since even a tract is so large that it is hard to be read into memory. In our case, the

[1]The reference catalogue is made by P. Price (private communication).

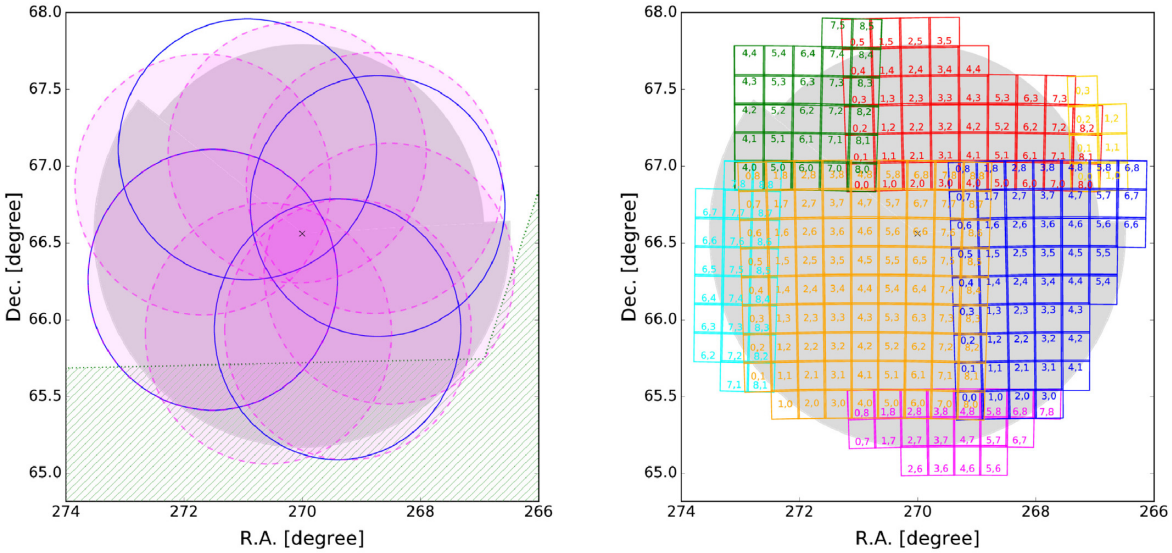

Figure 1. Field coverage maps of the AKARI NEP-Wide field survey and the Subaru/HSC following survey. Left: the AKARI NEP-Wide survey area is shown in the grey field, and the central coordinate is marked with a cross mark. The seven pink dashed–shadowed circles represent the HSC *r*-band observation area, while the four blue solid circles show the HSC *g*-, *i*-, *z*-, and *y*-band observation areas. The green hatched area is the SDSS survey region. Right: the tract and patch distributions. Each open square represents each patch field with its number. The different tract area is shown in different colour codes.

Table 1. Summary of our HSC observation, and the data quality.

Filter ($\lambda_{\rm eff}$) (Å)	Total exp. time (s)	Exp. time (*s*/field)	Seeing (arcsec)	5σ depth (AB mag)
g (4745)	27 440	6860	0.68	28.10
r (6178)	22 570	2010–4760	1.26	26.77
i (7659)	5360	1340	0.84	26.25
z (8898)	6480	1620	0.76	25.47
y (9762)	16 420	4105	0.74	25.04

sky regions of the *g*, *i*, *z*, and *y* bands acquired in four FoVs are split into 256, 253, 252, and 254 patches in seven tracts, respectively, and the sky regions of the *r* band acquired in seven FoVs are split into 264 patches in the same seven tracts. In this paper, we focus on the common 251 patches covered by all the five HSC bands. The coadd images are made for each patch in each band with a homogenized photometric zero-point of 27.0 mag/ADU. The detection of sources and flux measurements are performed on the coadd images.

The pipeline measures fluxes in several ways: point spread function (PSF), aperture, Kron, and CModel photometry (Bosch et al. 2018). Throughout this paper, we use CModel magnitudes because CModel magnitudes are designed to yield accurate fluxes and colours for galaxies. The HSC CModel algorithm is described in Bosch et al. (2018). It fits objects using both de Vaucouleurs and exponential profiles convolved with the PSF model. Then, the two results are linearly combined to find the best fit to the galaxy image. For compact objects, CModel magnitudes are asymptotically approaching PSF magnitudes. Besides, an analysis of CModel performance on simulated galaxies in Huang et al. (2018) indicates that CModel performs well (statistical scatter ∼0.22 mag) for photometry down to $i = 25$.

Full width at half-maximum (FWHM) values of the seeing derived in the coadd images in each band are summarized in Table 1. The values in all the bands but the *r* band are between 0.68 and 0.84 arcsec. For the *r* band, due to the instrumental trouble in 2014, there

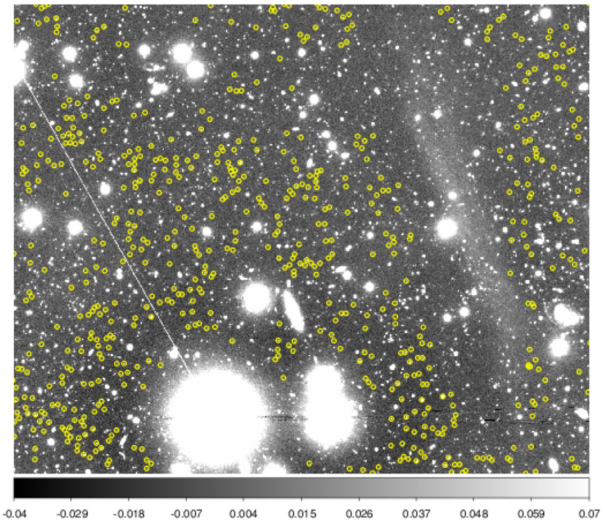

Figure 2. This is an example of the artificial structure located near the edge of HSC FoV. The vertically elongated structure can be seen on the right side of the figure. Detected HSC sources are marked in yellow open circles, and we can see that HSC sources are not detected around the elongated structure and bright stars.

was a big temperature gap between the instrument and the dome, and it made FWHM worse to 1.25 arcsec.

Due to the large *r*-band seeing compared to the other bands, some sources are culled when performing the multiband analysis in Section 2.4. Kim et al. (2020) reduced this effect by not using the *r* band for source detection. Although this detection failure tends to occur for fainter sources in the *r* band, it is not expected to impact this work because it is not a bias that selectively drops particular sources.

We mention here that many arc-shape ghosts appear near the edge of HSC FoV due to bright stars. These features cause no HSC source detection around them (see Fig. 2). Although we will cross-

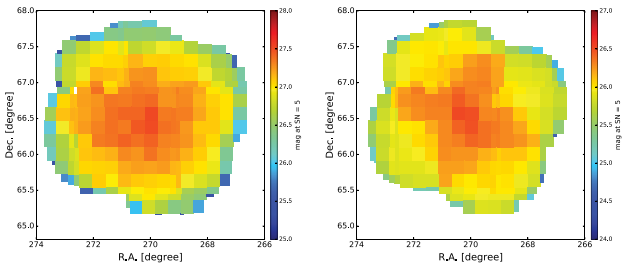

Figure 3. Examples of the 5σ limiting magnitude map for point sources in *r* (left) and *i* (right). The colour code represents the depth of magnitude at S/N = 5.

match between the HSC band-merged catalogue and an AKARI NEP-Wide band-merged catalogue in Section 3, we will fail to find HSC counterparts of AKARI NEP-Wide sources in these undetected HSC source regions. The sources are excluded from an AKARI-HSC band-merged catalogue that will be built in Section 3.2. Kim et al. (2020) use a recent version `hscPipe` to attempt to detect these damaged sources by the ghosts.

2.2 Detection limits

We determined the 5σ depth for point sources. The `hscPipe` outputs a parameter '`classification_extendedness`', which can be used to separate stars and galaxies in the images. We selected a point source with `classification_extendedness` = 0 and calculated the signal-to-noise ratios (S/Ns) of all the point sources for each patch based on its PSF fluxes and errors. Then, we derived the mean PSF magnitudes for sources with the S/Ns between 4.9 and 5.1. We performed this process for all the 251 patches. Fig. 3 shows examples of the 5σ depth map in the *r* and *i* bands. Our HSC data sensitivity vary with position of the sky due to the systematic changes in the depth of coverage. The sensitivity map in the *i* band shows a windmill-like pattern with four blades due to the four HSC FoVs. The distributions in the *g*, *z*, and *y* bands also show a similar pattern. On the other hand, the depth in the *r* band shows more like concentric distribution. Fig. 4 shows the 5σ depth against the sky regions, which are a sequential serial number of patches. We measured median 5σ limiting magnitudes of 28.10, 26.77, 26.25, 25.47, and 25.054 AB mag for the *g*, *r*, *i*, *z*, and *y* bands, respectively. The exposure time per field in the *g* band is longer and seeing is better compared with the HSC-SSP UltraDeep survey (Aihara et al. 2018). Thus, the 5σ depth for point sources in the *g* band is better. The exposure time per field in the *r* and *y* bands is between the approximate exposure times of the HSC-SSP Deep and UltraDeep surveys, while the exposure time in the *i* and *z* bands is between the exposure times of the HSC-SSP Wide and Deep surveys, and our 5σ depth magnitudes agree reasonably well with their 5σ depth. As mentioned by Aihara et al. (2018), the flux uncertainties obtained by `hscPipe` are somehow underestimated due to the covariance between pixels. This leads to an overestimation of the 5σ depth. We stress here that the relative depth relationship between our data and the HSC-SSP DR1 discussed above is correct since we have estimated the 5σ depth in the same way as Aihara et al. (2018).

2.3 Number count

We also investigated the number counts of the HSC sources. Fig. 5 shows the number of sources in every 1.0 mag in 1 sq. deg sky region derived from each patch in each band. The red stars in Fig. 5 show median value of the observed counts of galaxies. As a comparison of the number counts, we overplotted the results from the CFHTLS

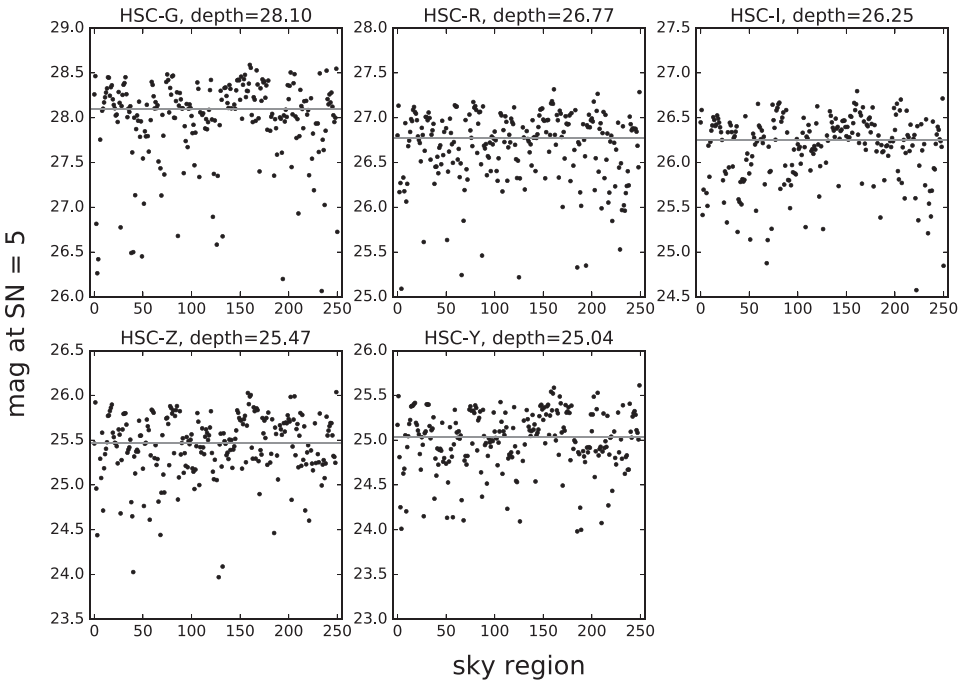

Figure 4. The 5σ limiting magnitudes for each patch (sky region) in each band. Panels from the top left to the bottom right show from the *g* to *y* bands, respectively. The horizontal axis shows 251 patches numbered consecutively from 0. The data points are the 5σ limiting magnitudes in each patch. The solid horizontal line shown in each panel indicates the median of 5σ limiting magnitudes for each band.

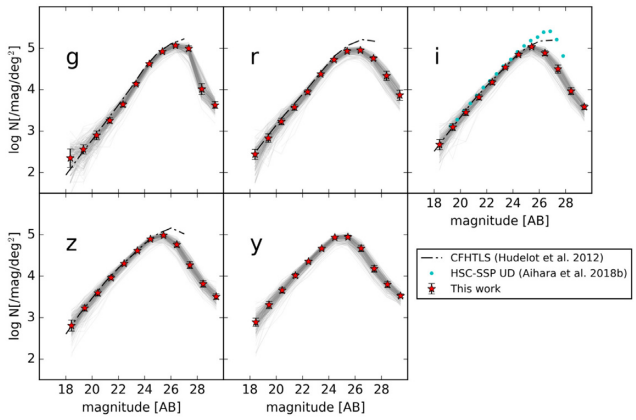

Figure 5. Number counts for the g, r, i, z, and y bands. The grey lines show the number counts in each patch and the red stars represent the 3σ clipped median values in all the patches. The dash–dot curves are showing the galaxy number counts from the CFHTLS T0007 data (MegaCam g', r', i', and z' bands; Hudelot et al. 2012) and the cyan circles in the i band are the result from the HSC-SSP UltraDeep catalogue (Aihara et al. 2018).

T0007[2] MegaCam data (dash–dot curve; Hudelot et al. 2012) in the g, r, i, and z bands and from the HSC-SSP UltraDeep catalogue (cyan filled circles; Aihara et al. 2018) in the i band. The figure shows that our results agree with the literature results down to the peaks.

2.4 Multiband analysis

Next, we performed a multiband analysis using the `hscPipe` in the regular procedure, which includes processes such as catalogue merging between bands, culling spurious detection on outskirts of bright objects, and photometric measurements using reference-band positions and shapes. Refer to Bosch et al. (2018) for details, and here we briefly explain the processes. The data reduction and photometric measurements so far were performed for each band separately. However, it may happen that an object is divided into deblended objects and photometric measurements are carried out on each of them, while the same object in the other bands is not deblended and the photometric estimation is carried out as a single object. In this case, the centroids and shapes of sources are different from band to band, and the measurement does not give good colours of sources. In order to maximize cross-band consistency in these measurements, the `hscPipe` can perform photometry with fixed positions and shape of sources across all five HSC bands. First, we prioritized the bands. Then, according to the priority, the `hscPipe` refers to the photometric measurement catalogue in the priority reference band and registered all the detected sources in the catalogue. In this work, we selected the g band as the highest priority filter because the quality of our g-band data is deeper than that of the other band data (see Fig. 4).

Then the `hscPipe` checked each object found in the second and subsequent priority bands, and added an object as a counterpart if its distance from the nearest registered object is less than 0.3 arcsec. If the distance between an object and the nearest registered source is more than 1 arcsec, the object is added as a new object. On the other hand, if the distance between an object and the nearest registered source is between 0.3 and 1 arcsec, the object is ignored because the source cannot be identified as the same object or a different object.

[2]https://www.cfht.hawaii.edu/Science/CFHLS/T0007/

All the data reduction by the `hscPipe` is performed for each and every patch separately. In the final step of this procedure, we combined the source lists in all the patches. Each patch overlaps with adjacent patches, which means that some sources located in the overlapping regions are duplicately detected. In order to avoid duplicated registration, we selected sources flagged as `detect_is-primary = True`, which lets us choose unique objects in the overlapping regions. We successfully registered 2 702 828 HSC sources in the five-band-merged catalogue. There are some sources whose fluxes cannot be derived by the CModel fitting procedure. In the following sections, we performed an SED fitting to a multiband catalogue, which includes the AKARI-HSC merged information as well as all available supplementary data, in order to perform the redshift estimation and galaxy classification. Because of the critical importance of the HSC photometric data in the processes, we removed sources for which CModel could not measure fluxes. As a result, 2605 316 objects are included in the HSC catalogue.

3 MULTIBAND MERGING

Kim et al. (2012) produced separated photometric catalogue for nine AKARI/IRC bands. In this work, we first carried out the band merging for the nine bands of AKARI and also for the five bands of HSC, respectively. Then, we build up a multiband catalogue from optical to far-IR by adding other supplementary data to the AKARI-HSC catalogue.

3.1 AKARI NEP-Wide nine-band-merged catalogue

For creating an AKARI NEP-Wide nine-band-merged catalogue, we cross-identified with position matching among three single-band catalogues in each channel. For example, the NIR channel, the $N2$, $N3$, and $N4$ single-band catalogues contain 87 857, 104 170, and 96 159 sources, respectively. Using a 3 arcsec searching radius used in Kim et al. (2012), we found 95 484 sources detected in at least two of the NIR single bands. We considered these sources as real objects and regarded the source list as a NIR combined catalogue. In the same manner, we made MIR-S and MIR-L combined catalogues including 16 766 and 9637 sources from $S7$ (15 359 sources), $S9W$ (18 772 sources), and $S11$ (15 680 sources) catalogues and from $L15$ (13 148 sources), $L18W$ (15 154 sources), and $L24$ (4018 sources) catalogues, respectively.

Next, we searched for pairs of sources between NIR and MIR-S channels by position matching with a 3 arcsec radius to build a NEP-Wide catalogue. In the matching process, we searched for counterparts between all the possible combinations of the six NIR and MIR-S bands and found 15 525 pairs. Since sources listed in one but not in both combined catalogues are still regarded as real sources, we put them into the NEP-Wide catalogue. There are 81 200 sources detected either of the NIR or MIR-S combined catalogues. We applied the same procedure for MIR-S and MIR-L and found 6001 pairs and 20 402 sourced detected in one of the combined catalogues, respectively.

Finally, we combined the results of cross-matching between NIR and MIR-S and between MIR-S and MIR-L. Consequently, we obtained the NEP-Wide nine-band-merged catalogue containing 100 361 sources. Coordinates of sources in the shortest band in which the sources are detected are adopted as representative coordinates for the AKARI NEP-Wide sources and used for the following merging processes.

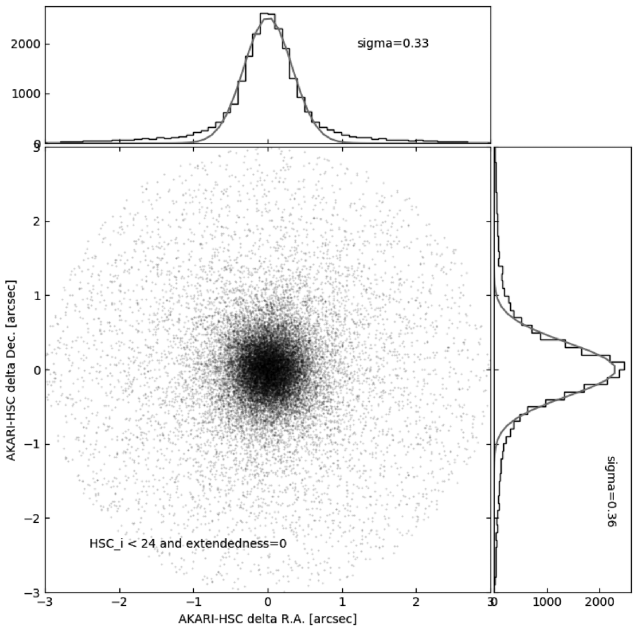

Figure 6. Comparison of astrometry between the AKARI and HSC catalogues.

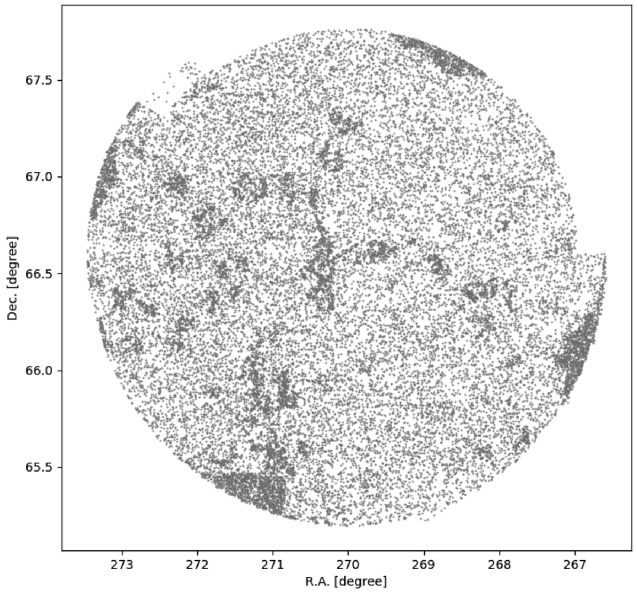

Figure 7. Spatial distribution of the NEP-Wide IR sources without HSC optical counterpart. There are four major regions at north–north-west, east–north-east, south–south-east, and west–south-west, where our HSC observations do not cover in the NEP-Wide field. There are filamentary dense regions inside the HSC observation field where the HSC images are damaged by artificial structures due to bright stars.

3.2 Cross-identification of AKARI and HSC data

We first estimated the relative positioning accuracy of the HSC and NEP-Wide catalogues. In order to find counterparts of the AKARI NEP-Wide sources in the HSC catalogue, we first estimated the relative positioning accuracy of the HSC and NEP-Wide catalogues. We selected HSC stars and used them for the estimation. Bosch et al. (2018) reported that `classification_extendedness` separates stars from galaxies well down to $i \sim 24$ mag. Then, we chose 87 979 stars from the 2.6 million HSC sources, with `classification_extendedness` $= 0$ and $i < 24$, and performed cross-matching with all the sources in the AKARI NEP-Wide catalogue, using a temporary search radius of 3 arcsec. Fig. 6 shows the relative positions of the samples. The root mean square (RMS) position errors in the R.A. and Dec. are 0.33 and 0.36 arcsec, respectively. Hence, we decided to use 1.45 arcsec, corresponding to the three times of their square sum root value, as the search radius for finding counterparts of AKARI NEP-Wide sources in HSC catalogue. With that cross-matching, we found 77 014 pairs. There are 4837 cases where multiple HSC objects are found within the search radius of a single AKARI object, and 1206 cases where a common HSC object is found within the search radius of multiple AKARI objects. In this work, we simply adopted the nearest pair as the counterparts, even in the multiple match cases. Finally, 70 959 AKARI-HSC pairs are listed in the AKARI-HSC catalogue.

The locations of 29 402 AKARI sources without HSC counterparts are shown in Fig. 7. Many of them are located in four regions outside of the HSC observation field, and a non-negligible number of sources are located around the central area of the NEP-Wide field. The area corresponds to the edge of each HSC FoV. As we mentioned in the previous section, there are sky regions damaged by artificial structures close to the edge of HSC FoV and no HSC sources are detected around them. These NEP-Wide sources without HSC counterparts inside the whole HSC observation field are due to the no HSC detection. Thus, the actual number of the optical-faint AKARI sources should be smaller than ∼30 000. Toba et al. (2020) studied the physical properties of these AKARI sources without HSC. In this paper, we focus on NEP-Wide sources with secure HSC counterparts.

3.3 Cross-identification of AKARI-HSC catalogue and supplementary data

We performed cross-matching between our AKARI-HSC catalogue and existing supplementary multiband data in the NEP-Wide field.

Photometric measurements of all the supplementary data but *WISE* and *Herschel* were performed in a Kron radius (Kron 1980) of SExtractor (Bertin & Arnouts 1996), which includes most of the source flux (> 90 per cent). Since most of the Wide-field Infrared Survey Explorer (WISE) and *Herschel* sources are unresolved, the photometric estimations were carried out using a PSF profile fit. This means that all the flux values in the following supplementary catalogues cover the majority of the source fluxes in each bandpass. Therefore, we do not apply any aperture corrections to the supplementary data.

In the following band-merge processes, we used the same method as used in the AKARI-HSC cross-match. We used the HSC stars and all objects in each supplementary catalogue to estimate the astrometric accuracy. We then used three times the RMS error for the catalogue matching. However, since *Herschel* (PACS and SPIRE) catalogues are likely to contain few stars, we used all AKARI-HSC objects and all *Herschel* objects to estimate the astrometric accuracies.

When multiple AKARI-HSC sources found a common supplementary source, it is difficult to determine whether the multiple sources are blended or only one source is detected in the supplementary catalogue. However, in either case, the measured flux in the supplementary catalogue is expected to be equal to or larger than the flux of each object. In this work, in order to perform SED fitting

using the supplementary data in the following sections, we regarded the measured flux as the upper limit of the supplementary object and registered it as the counterpart of all the multimatched AKARI-HSC sources.

3.3.1 *CFHT/MegaCam* u* *band*

In the AKARI NEP survey field, two individual observations using the CFHT/MegaCam with its u^*-band filter (3235–4292 Å with an effective wavelength of $\lambda_{\rm eff} = 3827.2$ Å) were carried out. The first observation carried out over the NEP-Deep field covering about 1 sq. deg (Takagi et al. 2012; Oi et al. 2014). 55 145 sources are listed in the u^*-band catalogue (u_{14}), and 5σ limiting magnitudes of the catalogue are 24.6 mag. After the HSC observations, a new CFHT MegaPrime/MegaCam observation with a new u-band filter in the AKARI NEP-Wide field was performed to observe the remaining 3.6 sq. deg of the NEP-Wide field that was not covered by the first u^*-band observation (Huang et al. 2020). 351 579 sources are listed in the new u-band catalogue (u_{20}) and 5σ limiting magnitudes of the catalogue are 25.8 mag.

We cross-matched the AKARI-HSC catalogue with both the u_{14} and u_{20} catalogues individually. Since the astrometric differences between the AKARI-HSC catalogue and the u_{14} and u_{20} catalogues are 0.168 and 0.185 arcsec, respectively, the actual search radii used for cross-identifications were 0.503 and 0.555 arcsec, respectively. 9152 sources are identified in the u_{14} catalogue and 27 355 sources are in the u_{20} catalogue. All the counterparts are found uniquely within the searching area around AKARI-HSC sources. 1506 sources are detected in both the u_{14} and the u_{20} catalogues, and we decided to use their photometric data from the u_{20} because the limiting magnitude of the catalogue is better than the u_{14}. Finally, 35 001 u- or u^*-band sources are merged as the counterparts of the AKARI-HSC sources.

3.3.2 *KPNO 2.1-m/FLAMINGOS* J *and* H *bands*

Jeon et al. (2014) presented observations with FLoridA Multiobject Imaging Near-IR Grism Observational Spectrometer (FLAMINGOS; Elston et al. 2006) at the Kitt Peak National Observatory (KPNO) 2.1 m telescopes, and created a source catalogue in the J and H bands covering the AKARI NEP-Wide field. The brief summary of the catalogue is as follows: it covers 5.1 sq. deg, it achieves the detection limits of $J \sim 21.6$ and $H \sim 21.3$ AB mag in 5σ, and 208 020 and 203 832 sources are detected in the J and H bands, respectively. We again used a 1.5 arcsec temporal search radius for the cross-matching between the AKARI-HSC catalogue and the FLAMINGOS catalogue to measure the relative astrometric accuracy. The RMS position error is 0.219 arcsec, and then the search radius for the cross-identification between the catalogues is 0.658 arcsec. 46 856 and 48 417 counterparts are identified in the J and H bands, respectively. All the FLAMINGOS counterparts are uniquely identified.

3.3.3 *CFHT/WIRCam* Y, J, *and* K_s *bands*

Oi et al. (2014) described CFHT/WIRCam Y, J, and K_s observations covering a 47 arcmin × 44 arcmin area in the NEP-Deep field. Although the data cover only ∼10 per cent of the NEP-Wide field, we merged the data into the multiband catalogue because the band set fills the gap between the HSC optical to AKARI NIR bands. The 4σ detection limits reach to 23.4, 23.0, and 22.7, and 39 063, 34 138, and 38 053 sources are detected in the Y, J, and K_s bands, respectively. Since the RMS positional error for the near-IR catalogue was found to be 0.168 arcsec, we used a search radius of 0.504 arcsec for the catalogue merging. 7714, 7742, and 7954 counterpart sources are identified in the Y, J, and K_s bands, respectively. All of the counterparts are found uniquely within the search area from AKARI-HSC sources.

3.3.4 *WISE W1, W2, W3, and W4*

The *WISE* mission surveyed the whole sky in four bands, namely *W1* (3.4 μm), *W2* (4.6 μm), *W3* (12 μm), and *W4* (22 μm), with spacial resolutions of 6.1, 6.8, 7.4, and 12.0 arcsec, respectively. In this paper, we adopted the *AllWISE* catalogue data release (Cutri et al. 2014). According to the Explanatory Supplement to the *AllWISE* Data Release Products,[3] the *AllWISE* data release includes data from the *WISE* Full Cryogenic, three-Band Cryogenic, and the Near-Earth Object Wide-field Infrared Survey Explorer (*NEOWISE*) Post-Cryo survey phases. The *AllWISE* catalogue contains astrometry and photometry for almost 748 million objects, which are both point-like and extended objects. *WISE* sensitivity varies with position of the sky due to systematic changes in the depth of coverage and the region around the NEP is one of the best sensitivity areas thanks to the high visibility for space missions. The 5σ photometric sensitivities at around the NEP for the *W1*, *W2*, *W3*, and *W4* are 18.70, 17.38, 12.54, and 8.90 in the Vega system, which correspond to 10.0, 18.7, 298, and 2249 μJy or 21.40, 20.72, 17.71, and 15.52 AB mag, respectively. Since the *WISE* catalogue adopts the Vega magnitude system ($m_{\rm Vega}$), we converted it into the AB magnitude system ($m_{\rm AB}$), using magnitude offsets Δm of 2.699, 3.339, 5.174, and 6.620 for the *W1*, *W2*, *W3*, and *W4* bands, respectively, in $m_{\rm AB} = m_{\rm Vega} + \Delta m$.

We used the PSF profile-fitting magnitude (`w1-4mpro`) as the magnitude for the majority of the *WISE* sources because most objects in the *AllWISE* catalogue are unresolved. However, because the `w1-4mpro` photometry is optimized for point sources and may underestimate the true brightness of extended sources, we used the elliptical aperture magnitude (`w1-4gmag`) for the extended sources. The aperture is based on the elliptical shape reported in the Two Micron All Sky Survey Extended Source Catalog. We defined extended sources using `ext_flg` in the *AllWISE* catalogue. We do not use the `w1-4mpro` magnitude if the uncertainty is the missing value (`w1-4sigmpro` = nan) because the magnitude might not measurable. Then, we checked whether sources are saturated in bands. The saturation levels in *W1*, *W2*, *W3*, and *W4* are 8, 7, 4, and 0 mag, respectively. We do not use the magnitudes in any band that exceed the saturation level in that band. We also checked whether the sources are contaminated by image artefacts (e.g. diffraction spikes, scattered-light haloes, or optical ghosts) according to `cc_flags` in the *AllWISE* catalogue. The `cc_flags` is a four-character string and each character is a flag for each band. We do not use the magnitudes in any band if the `cc_flags` values in that band are non-zero characters. An extended source is flagged as `w1-4gflg` = 0 if any image pixel in the elliptical measurement aperture is no problem (e.g. not confused with nearby objects, or not contaminated by saturated or otherwise unusable pixels, or is an upper limit). We thus do not use the magnitudes in any band with `w1-4gflg` ≠ 0. After the checking the magnitudes with the saturation levels and the photometric quality flags, we eliminated sources with no valid magnitudes in any band. Using a 1.5 arcsec

[3] http://wise2.ipac.caltech.edu/docs/release/allwise/expsup/

temporal search radius, we found that the RMS position error between the AKARI-HSC catalogue and this *ALLWISE* catalogue is 0.257 arcsec. We then cross-matched between the catalogues with a 0.769 arcsec search radius, and identified 38 419, 36 547, 8062, and 2142 *WISE* sources in the *W1*–*W4* bands, respectively, as the counterparts of the AKARI-HSC sources. These three *WISE* sources are listed in the catalogue as counterparts of both AKARI-HSC sources, with flags indicating that each *WISE* flux is the upper limit.

3.3.5 Spitzer*/IRAC 3.6 and 4.5 μm*

Nayyeri et al. (2018) presented a photometric catalogue of the NEP field with *Spitzer* Space Telescope/IRAC. The observation was carried out in 3.6 and 4.5 μm bands during the warm mission over an area of 7.04 sq. deg that covers almost all the NEP-Wide field. The 1σ depth measured with a 4 arcsec aperture in diameter in the 3.6 and 4.5 μm band is 1.29 and 0.79 μJy, respectively. A temporal search radius of 1.5 arcsec was used for the RMS position error estimation between the AKARI-HSC catalogue and this *Spitzer* catalogue. Since the value is found to be 0.193 arcsec, three times that value, 0.580 arcsec, are used for cross-identification between the catalogues. Then, 54 313 and 54 324 *Spitzer* sources in 3.6 and 4.5 μm bands, respectively, are found as counterparts of the AKARI-HSC sources. All of the *Spitzer* counterparts are found uniquely within the search area from AKARI-HSC sources.

3.3.6 Herschel*/PACS and SPIRE*

The AKARI NEP-Wide field was also observed by both *Herschel*/PACS (OT1-sserj01-1, PI: S. Serjeant; Pearson et al. 2017) and SPIRE (OT2-sserje01-2, PI: S. Serjeant; Burgarella et al. 2019; Pearson et al. 2019). PACS observations were made simultaneously in the 100 μm band (green) and 160 μm band (red) covering most of the AKARI NEP-Deep field, while SPIRE observations were carried out in 250 μm band (PSW), 350 μm band (PMW), and 500 μm band (PLW) covering the entire AKARI NEP-Wide field. The rms noise values at 100, 160, 250, 350, and 500 μm are ∼1.5, 8, 9.0, 7.5, and 10.8 mJy, respectively, which are higher than the extragalactic confusion limits determined by Magnier et al. (2013) of 0.75 and 3.4 mJy at 100 and 160 μm and Nguyen et al. (2010) of 5.8, 6.3, and 6.8 mJy at 250, 350, and 500 μm, respectively. The FWHMs of the PSFs for 100, 160, 250, 350, and 500 μm are 6.9, 11.3, 19.1, 28.7, and 39.5 arcsec, respectively. The fluxes of the PACS and the SPIRE samples are estimated using a PSF fitting algorithm (DAOPHOT) that is adapted to confused data even though the PACS and the SPIRE data are above the confusion limits. Thus, the impact of confusion in the *Herschel* data is considered as not significant. We carried out cross-matching between all the AKARI-HSC sources and each PACS and SPIRE catalogue with a temporal search radius of 2.5 and 4 arcsec, respectively, and found that the RMS position error is 0.917 and 2.814 arcsec, respectively. Thus, 2.754 and 8.441 arcsec are adopted as search radii for cross-identify with PACS and SPIRE catalogue, respectively. 776, 467, 2202, 1983, and 802 sources in 100, 160, 250, 350, and 500 μm are identified, respectively. Most of the PACS sources are matched to only one counterpart, and there are nine cases where two AKARI-HSC sources share a common PACS source. On the other hand, there are 396 cases where 2 AKARI-HSC sources are found within the search radius from a SPIRE source. In 34 cases, 3 AKARI-HSC sources are found within the search radius from a SPIRE source, and in 3 cases, 4 AKARI-HSC sources are found within the search radius of a SPIRE source. For all of the multimatching cases, we listed the fluxes of the *Herschel* sources as upper limits.

Table 2. The Galactic extinctions and the systematic shifts among the different bandpass applied for the photometric redshift estimation.

Filter	The Galactic extinction	Systematic offset
MegaCam *u*	0.220	−0.005
HSC *g*	0.170	−0.146
HSC *r*	0.125	−0.214
HSC *i*	0.092	−0.265
HSC *z*	0.070	−0.241
HSC *y*	0.060	−0.216
WIRCam *Y*	0.056	−0.067
WIRCam *J*	0.040	−0.010
WIRCam K_s	0.017	0.133
FLAMINGOS *J*	0.041	0.116
FLAMINGOS *H*	0.026	0.169
AKARI *N*2	–	0.146
AKARI *N*3	–	0.047
AKARI *N*4	–	−0.060
WISE W1	–	0.104
WISE W2	–	−0.076
Spitzer 3.6 μm	–	−0.072
Spitzer 4.5 μm	–	−0.240

4 PHOTOMETRIC REDSHIFT CALCULATION

To compute photometric redshifts ($z_{\rm phot}$), we used an SED fitting code LE PHARE (Ilbert et al. 2006, 2009; Arnouts et al. 2007) for at most 18 optical to near-IR (< 7 μm) photometric data, MegaCam u^*, HSC *g*, *r*, *i*, *z*, *y*, WIRCam *Y*, *J*, K_s, FLAMINGOS *J*, *H*, AKARI/IRC *N*2, *N*3, *N*4, *WISE W1*, *W2*, and *Spitzer*/IRAC 3.6 and 4.5 μm. We applied corrections for the Galactic extinction at around the NEP for our optical and near-IR data based on the Schlegel, Finkbeiner & Davis (1998) extinction map [reddening at NEP: $E(B-V) = 0.046$] and the Cardelli, Clayton & Mathis (1989) extinction law with an assumption of a total-to-selective extinction ratio $R_{\rm v} = 3.1$. The Galactic extinctions in each filter we used are summarized in Table 2. We utilized empirical galaxy templates from Coleman, Wu & Weedman (1980) and two starburst templates from Kinney et al. (1996) with an extrapolation and an adjustment to match spectra taken in the deep survey using the VIsible Multi-Object Spectrograph (VIMOS) on the Very Large Telescope (VLT) (Arnouts et al. 2007). Since these templates do not contain AGN templates, we added nine hybrid templates of AGN (TQSO1) and the host galaxy (IRAS 22491-1808) constructed in Salvato et al. (2009). The AGN and host galaxy templates are both included in the *Spitzer* Wide-Area Infrared Extragalactic survey (SWIRE) template (Polletta et al. 2007),[4] and are combined in varying proportions from 90:10 to 10:90 (see for details on these templates). Extinction law from Calzetti et al. (2000) with reddening $E(B-V)$ of 0.0, 0.025, 0.05, 0.075, 0.1, 0.15, 0.2, 0.3, 0.4, 0.5, 0.6, 0.7, 0.8, 0.9, and 1.0 is adopted.

Photometric redshift estimation by the χ^2 template fitting only works well if the colour–redshift relation predicted from the template represents the observed colour–redshift relation. However, as demonstrated by Ilbert et al. (2006, 2009), systematic offsets are often found between the best-fitting SED templates and the observed magnitudes in a given filter. Uncertainties in the zero-point

[4] http://www.iasf-milano.inaf.it/~polletta/templates/swire_templates.html

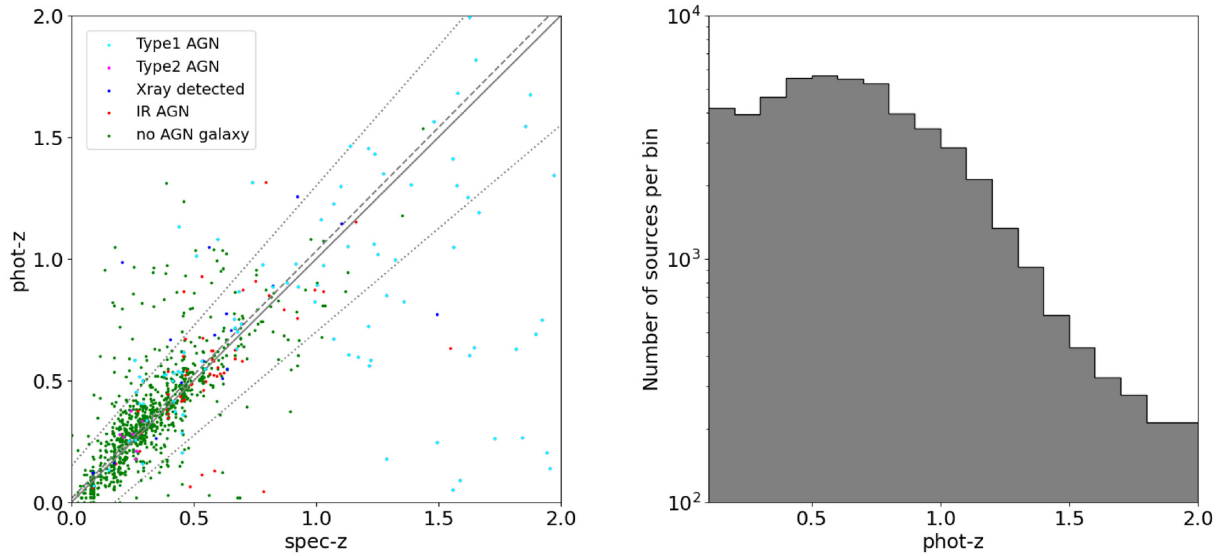

Figure 8. Left: photo-z versus spec-z at $0 < z < 2.0$ for all the 1087 spectroscopic sources with colour codes as follows: cyan: Type1 AGNs, pink: Type2 AGNs, blue: X-ray sources, red: IR AGNs, and green: galaxies (no AGNs). The solid line is photo-z = spec-z. The dashed line shows the systematic offset between $z_{\rm phot}$ and $z_{\rm phot}$ (0.013). The pair of the dotted lines represents $(z_{\rm phot} - z_{\rm spec})/(1 + z_{\rm spec}) = \pm 0.15$. The photometric redshift dispersion σ and the catastrophic error rate η at $z < 1.5$ are 0.060 and 13.4 per cent, respectively. Right: redshift distribution of the entire AKARI-HSC sample at $0 < z < 2.0$.

calibration of the photometric data as well as imperfect knowledge of galaxy SEDs are responsible for these offsets, and must be corrected. For example, we have two J-band photometric data sets using FLAMINGOS and WIRCam. Those catalogues have an ∼0.075 mag systematic offset from each other. To evaluate the zero-point errors, we used an option AUTO_ADAPT in the LE PHARE for sources that have spectroscopic redshifts. Many spectroscopic observations with various telescopes/instruments in optical and near-IR wavelength were carried out in the NEP-Wide survey field, Keck/DEIMOS (Kim et al. 2018; Shogaki et al. 2018), MMT/Hectospec (Shim et al. 2013), WIYN/Hydra (Shim et al. 2013), GTC (Miyaji et al. in preparation), and near-IR, Subaru/FMOS (Oi et al. 2017). Spectroscopic redshifts for 3084 sources were measured altogether. From the spectroscopic sample, we selected 1087 galaxies with a secure spec-z measured with more than two emission lines or absorption lines. 117 sources are broad-line Type1 AGNs, and 7 sources are Type2 AGNs classified by their emission line ratios. 39 out of the 1087 spectroscopic sample are detected in the *Chandra*/X-ray observation in the NEP-Deep survey field (Krumpe et al. 2015). Of the 39 sources, 19 are Type1 AGNs with the wide emission lines mentioned above. Hanami et al. (2012) distinguished star-forming galaxies from AGN-dominated galaxies in the AKARI NEP-Deep survey catalogue using a colour diagnostic approach (IR AGN). 54 sources in our spectroscopic sample are included in the IR-AGN categories. The other 896 spectroscopic sources do not show signs of AGN in the existing data sets.

For the optimization of the colour–redshift relations between the predicted from the model templates and the observed data, we first fixed their $z_{\rm spec}$ values and let the code find the best-fitting templates for each spectroscopic sample. A difference between the predicted flux from the best-fitting template and the observed flux in each photometric band for each spectroscopic sample is calculated. The average of the differences in each band should be ∼ 0. Thus, the average values are systematic offsets. After the systematic offsets were removed, the same processes were iteratively performed. The systematic offset values converged after four iterations. The systematic offsets listed in Table 2 were applied to all the photometric data when calculating the $z_{\rm phot}$ for all the AKARI-HSC sources.

We used photometric redshift dispersion $\sigma_{\Delta z/(1+z_{\rm s})}$ and the outlier rate η to assess the photometric redshift accuracy by comparing it with the spectroscopic redshifts. The photometric redshift dispersion is defined using the normalized median absolute deviation $\sigma_{\Delta z/(1+z_{\rm s})} = 1.48 \times {\rm median}(|\Delta z|/(1 + z_{\rm s}))$ (Hoaglin, Mosteller & Tukey 1983). The outlier rate is conventionally defined as the proportion of objects $\eta = \frac{N(|\Delta\ z| > 0.15)}{N_{\rm total}}$.

The left-hand panel of Fig. 8 shows the comparison between $z_{\rm phot}$ and $z_{\rm spec}$ for all the 1087 spectroscopic sources. At $0.2 < z < 1.5$ where most of the spec-z sources are distributed, the systematic offset, photometric redshift accuracy, and outlier rate are 0.013, 0.060, and 13.4 per cent, respectively. Fig. 8 shows that photo-z of the broadened-line Type1 AGNs is widely spreading out and not well determined. This is not surprising because power-law shape SEDs of AGN-dominated galaxies (i.e. Type1 AGN) do not have the distinctive SED shape from stellar emission such as the 4000 Å break, and/or the 1.6 μm bump that is useful for the photometric redshift estimation. About 25 per cent [=5/(39–19)] of the X-ray-detected sources are distributed outside of the $|\Delta z| < 0.15$ lines. X-ray is a good indicator to identify unobscured AGNs. Thus, the X-ray sources are probably unobscured AGNs and the emission from the AGNs dominates in optical wavelength. Hence, their photometric redshifts are not well estimated due to the same reason as the broadened-line Type1 AGNs. On the other hand, Type2-AGN, IR-AGN, and no-AGN galaxies where stellar emission is dominated in optical wavelength distribute along the line of $z_{\rm phot} = z_{\rm spec}$ within the $|\Delta z| < 0.15$. The photometric redshift accuracy and the outlier rate for Type2-AGN, IR-AGN, and no-AGN galaxies (i.e. AGN-undominated sources in optical) at $0.2 < z < 1.5$ reduced to $\sigma_{\Delta z/(1+z_{\rm s})} = 0.055$ and $\eta = 11.2$ per cent, respectively.

This photometric accuracy is slightly worse at low-z (<1) but better at high-z (>1) compared with the results by Oi et al. (2014) for NEP-Deep field ($\sigma \sim 0.032$ with $\eta \sim 5.8$ per cent for $z < 1$ and $\sigma \sim 0.117$ with $\eta \sim 16.6$ per cent for $z > 1$). This could be explained

by the difference of band set used for the photo-z calculation. Oi et al. (2014) used WIRCam Y-, J-, and K_s-band data in near-IR range. On the other hand, most of our sources do not have the WIRCam band data because the WIRCam observation covers only ∼10 per cent of the AKARI NEP-Wide field. Thus, for the sources located outside of the WIRCam observation field, we used FLAMINGOS J and H, AKARI NIR three bands, *WISE*, and *Spitzer* in near-IR range. K_s-band data play an important role in reproducing 1.6 μm stellar bump feature for low-z sources, which is usually used to estimate photo-z. The feature shifts towards longer wavelength and falls into AKARI $N2$ and/or $N3$ bands for sources at $z > 0.7$. Then, we can expect to improve the photometric redshift accuracy at high-z (>0.7). In addition, the improvement of the $z_{\rm phot}$ at high-z compared with Oi et al. (2014) is also thanks to the redshift reference sample. The Subaru/FMOS data from Oi et al. (2017) that provided spectroscopic redshifts at $z \sim 1$ helped us to estimate the magnitude zero-points more accurately, especially near-IR photometric data. Then, again the 1.6 μm stellar bump feature can be captured well for sources at high-z and the $z_{\rm phot}$ can be determined with high accuracy. Tanaka et al. (2018) computed photo-z for HSC-SSP Data Release 1, and achieved a typical accuracy of $\sigma \sim 0.05$ with $\eta \sim 15$ per cent at $0.2 \leq z_{\rm photo} \leq 1.5$. Although our photo-$z$ accuracy $\sigma_{\Delta z/(1+z_s)}$ is worse than that for the HSC-SSP Data Release 1, the difference seems insignificant. Moreover, the outlier rate is consistent thanks to the near-IR data. In the following sections, we discuss the evolution of the fraction of AGNs in the AKARI-HSC sample into four categories (quiescent, star forming, Type1 AGN, and Type2 AGN). However, as we have just shown, the accuracy of photo-z determinations for Type1 AGNs is not as good as for the other categories, so we will present the results both including and excluding Type1 AGNs.

The photometric redshift distribution of the AKARI-HSC sample between $0 < z < 2$ is shown in the right-hand panel of Fig. 8. Although stars for which redshift is 0 are included in the AKARI-HSC catalogue, we excluded them from here. Our AKARI-HSC galaxy sample peaks at $z \sim 0.6$, and the number of sources gradually decreases after that.

5 SED FITTING AND GALAXY TYPE CLASSIFICATION

5.1 Galaxy classification

In this section, we classify our AKARI-HSC sources into representative galaxy types by performing the template fitting using all the available multiwavelength data by the LE PHARE code with χ^2 minimization. We used a semi-empirical galaxy template library from the SWIRE (see Polletta et al. 2007, for the details of these templates). The library contains 25 model templates including 3 elliptical galaxies (models 1–3 in Table 3 and in Fig. 9), 7 spiral galaxies (models 4–10), 5 starbursts (models 11–15), 4 Type1 AGNs/QSOs (models 25–28), and 6 Type2 AGNs/QSOs (models 29–34), which cover the wavelength range between 0.1 and 1000 μm. Although the library already includes nine AGN templates, those templates are from spectra of nearby galaxies where the nuclear flux is well sampled, but the host galaxy is not fully included in slits or fibres. However, our photometric data include flux from the whole galaxy. Thus, SEDs of AGNs, which have a larger contribution from the host galaxy relative to the nuclear emission component, should be included in the SED model template library. Hence, we added the nine hybrid SEDs of an AGN and a host galaxy used for the photo-z estimation in Section 4 to the galaxy template library for galaxy classification (models 16–24).

Table 3. Summary of the number of AGNs and total galaxies in each $L_{\rm IR}$ bin and redshift bin. The numbers in the brackets include Type1 AGNs.

ID	Name[a]	Type	New category
1	Ell13	Ell ($t = 13$ Gyr)[b]	Quiescent
2	Ell5	Ell ($t = 5$ Gyr)[b]	”
3	Ell2	Ell ($t = 2$ Gyr)[b]	”
4	S0	S0[b]	Star forming
5	Sa	Spiral a[b]	”
6	Sb	Spiral b[b]	”
7	Sc	Spiral c[b]	”
8	Spi4	”	”
9	Sd	Spiral d[b]	”
10	Sdm	Spiral dm[b]	”
11	N6090	Starburst[b]	”
12	M82	””	”
13	Arp220	Starburst/ULIRG[b]	”
14	I20551	”	”
15	I22491	”	”
16	I22491-90_TQSO1-10	Hybrid[c]	Type1 AGN
17	I22491-80_TQSO1-20	”	”
18	I22491-70_TQSO1-30	”	”
19	I22491-60_TQSO1-40	”	”
20	I22491-50_TQSO1-50	”	”
21	I22491-40_TQSO1-60	”	”
22	pl_I22491-30_TQSO1-70	”	”
23	pl_I22491-20_TQSO1-80	”	”
24	pl_I22491-10_TQSO1-90	”	”
25	TQSO1	Type-1 QSO[b]	”
26	QSO1	”	”
27	BQSO1	”	”
28	Mrk231	Seyfert 1, BAL QSO + Starburst/ULIRG	”
29	N6240	Starburst/Seyfert 2[b]	Type2 AGN
30	Sey18	Seyfert 1.8[b]	”
31	Sey2	Seyfert 2[b]	”
32	I19254	Starburst/ULIRG[b] + Seyfert 2	”
33	QSO2	Type-2 QSO[b]	”
34	Torus	Type-2 QSO[b]	”

Notes. [a]Names in the original literature.
[b]Polletta et al. (2007).
[c]Salvato et al. (2009).

Since the SWIRE template covers a wavelength range of up to 1000 μm, we also used the templates as far-IR templates to measure the far-IR luminosity ($L_{\rm IR}$). However, the templates are based on actual observational data, and there is a great deal of variety due to the complex nature of the original sources on which it is based. Then, we tested a better far-IR model template by also using the far-IR templates by Dale & Helou (2002, hereafter DH02), which are simplified by modelling, independently. The DH02 library contains 64 model templates with different ratios of 2 far-IR flux densities at 60 and 100 μm. Moreover, we used 154 stellar templates including main-sequence stellar SEDs from Pickles (1998) and white dwarf SEDs from Bohlin, Colina & Finley (1995). All the SED fitting adopted the $z_{\rm phot}$ obtained in Section 4 to reduce the number of fitting parameters.

LE PHARE calculates the best χ^2 values from stellar libraries ($\chi^2_{\rm star}$) and galaxy libraries ($\chi^2_{\rm gal}$) separately for each source. We considered sources with smaller $\chi^2_{\rm star}$ than $\chi^2_{\rm gal}$ as stars. Indeed, 18 182 sources in the AKARI-HSC catalogue are classified as stars by the SED fitting and are excluded from the following discussions. We briefly tested the consistency between the star/galaxy classification by SED fitting and by morphology.

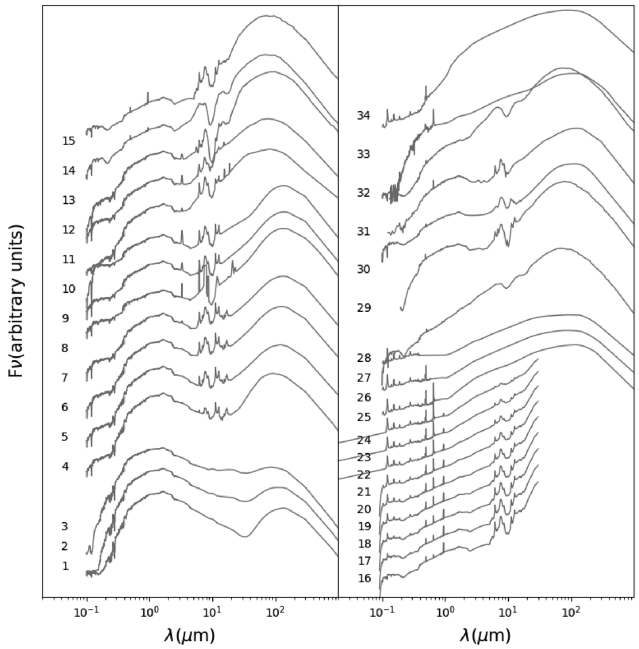

Figure 9. SED templates used for the galaxy classification. The numbers on the left of SED templates correspond to the IDs in Table 3.

As mentioned in Section 3.2, the `classification_extendedness` parameter can be used to distinguish between stars and galaxies for objects brighter than $i = 24$ mag. Of the 18 182 SED stars, 17 530 have valid i-band magnitudes, and all of them are brighter than $i = 24$ mag. Of the 17 530, 15 817 objects ($\sim$90 per cent) have `classification_extendedness` $= 0$, which means that they are morphologically classified as stars. This suggests that the classification of stars and galaxies by SED model fitting has been successfully achieved.

In the star-excluded galaxy subsample (52 777 sources), there are sources that are not detected at all, or only in one band, at wavelengths longer than rest-frame 7 μm. Since the $L_{\rm IR}$ cannot be estimated for such galaxies, we estimated the $L_{\rm IR}$ for only 8271 AKARI-HSC galaxies.

For the classification of galaxies, we use a simple approach – we adopt a class of the best-fitting model with the lowest chi-square. In Polletta et al. (2007), the 25 models were classified into 6 classes (elliptical, spiral, starburst, Type1 AGN, Type2 AGN, and composite of starburst and AGN). However, the classes are depending on the classification of the objects on which the models were based, and the shapes of the SEDs in the models between the classes are not well distinguished from each other. If similarly shaped SEDs belong to different classes, both models can reproduce the observational data equally well, and the results of the classification can easily change due to photometric indeterminacy and photo-z indeterminacy. In order to avoid this, the shape of the models belonging to each class should be well differentiated.

We reclassified the six classes in Polletta et al. (2007) into four new categories (quiescent, star forming, Type1 AGN, and Type2 AGN). The quiescent category includes three models (models 1–3) that belonged to the original elliptic class but are not active in star formation. 'Star forming' is a category that includes 12 models (models 4–15) that initially belonged to the spiral and starburst classes, which are active in star formation but not in AGN. Type1 AGN is a category of objects that are dominated by AGN emission in the optical wavelengths, and contains 13 models, including 4 models originally classified as Type1 AGN (models 25–28) by Polletta et al. (2007) and 9 hybrid models (models 16–24). Since the hybrid models are based on QSO models that were originally classified as Type1 AGN, and since the SED models in Fig. 9 show a power-law shape in the optical, we classified them as Type1 AGN instead of the Type2-AGN class shown next. The Type2-AGN category, which includes AGN activity but shows sufficient emission from the host galaxy in the optical band, contains six previously classified models into the original Type2 AGN and composite classes (models 29–34). The new categories are summarized in Table 3. Even for objects that cannot be successfully reproduced by any of the models, the 'best model' can be mathematically defined as a minimum chi-square value. In order to avoid misclassification of the galaxies by the 'best model', the significance level of a chi-square distribution is set at 5 per cent, and sources with the best model chi-square higher than the 5 per cent level are excluded from the following discussion. For the galaxy model fitting, we adopted 45.0 at 31 degrees of freedom (= total number of filters) and 22.4 at 13 degrees of freedom (= number of wavelength bands longer than 7 μm) as the critical values for the far-IR model fitting.

The SED fitting results are shown in Fig. 10. The rest-frame SEDs of objects classified into each category normalized by flux at 5500 Å are plotted as grey dots. For those data, we calculated the mean value at each 0.05 dex wavelength to estimate a representative SED for each category (orange triangle with 1σ error bars). As shown in the figure, the representative SEDs for all galaxy categories seem to be well reproduced by the galaxy model (SWIRE model) in the optical to mid-IR and by both the SWIRE and DH02 templates in the mid-IR to far-IR. This indicates that the galaxy type classification by SED fitting has been successful. As a result, 1684, 16221, 1591, 7354, and 1786 sources are classified as quiescent, star forming, Type1 AGN, and Type2 AGN, respectively.

We have 39 AKARI-HSC sources that are detected in X-ray (see Section 4), and 31 of which are fitted with chi-squared below the critical value. 59.4 per cent (19 sources) of the X-ray are classified as either Type1 AGN or Type2 AGN and the remaining 40.4 per cent of the X-ray sources show star-forming galaxy SEDs (star-forming category). This fraction is higher than the recovery rate obtained by Huang et al. (2017) based on SED fitting using photometric data with less than 18 bands for X-ray data. Of the 137 broad-line AGNs, 108 objects that were well fitted were classified as 82.6 per cent AGNs and the remaining 17.6 per cent as star-forming galaxies. Although the accuracy of photo-z determinations for broad-line AGNs was not very high, the classification seems to perform well because the shape of the SEDs characteristic of AGNs is different from that of the SEDs of normal galaxies. Among the seven Type2 AGNs, only three AGNs were found to be successfully fitting. Two of them are classified as Type2 AGNs, and the other one is classified as a star-forming galaxy.

Fig. 11 shows the distributions of redshift of each category. Majority of our AKARI-HSC sources are reproduced by templates of star-forming galaxies in the whole redshift range for $z < 2.0$. The peak of the photo-z distribution of the star-forming galaxy is around 0.6, consistent with that of the whole sample. On the other hand, the photo-z distribution peak for Type2 AGN is slightly off and is located at around $z = 1$. As described in Section 4, although the photo-z accuracy of Type1 AGN is not as good as that of other sources, the AGN's photo-z peak, including the Type1 AGN, is still around 1. The redshift of this peak is consistent with that of the photo-z distribution of the X-ray-selected AGN sample (Polletta et al. 2007).

The following discussion is based on the four categories classified by the best-fitting model. By dividing the categories into four broad

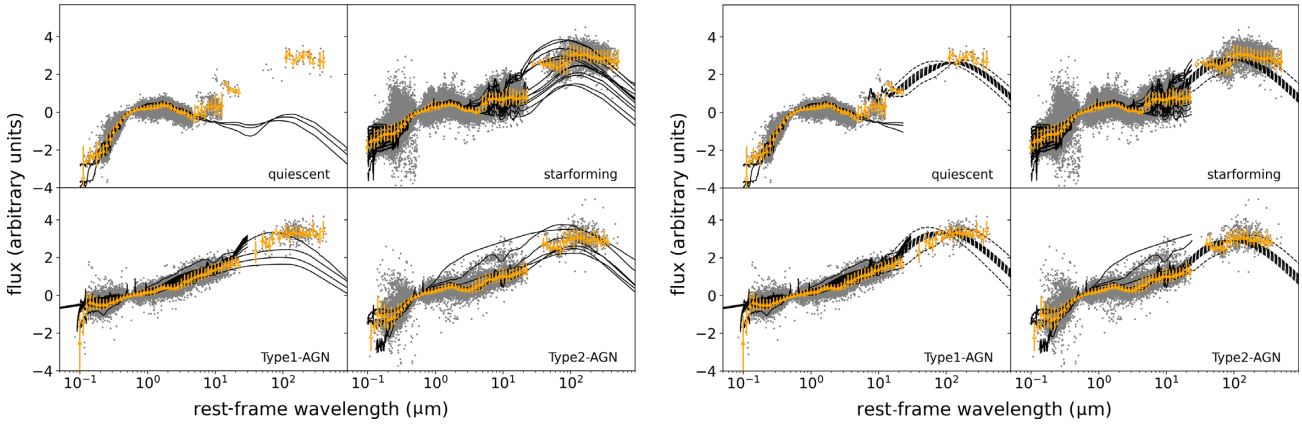

Figure 10. Rest-frame SEDs of the AKARI-HSC sources (grey dots) divided by the four galaxy categories, and normalized at the 0.55 μm. The mean values of the data in each 0.05 dex bin of wavelength are plotted in triangles with 1σ error. The galaxy model templates for each category and the far-IR templates (left: SWIRE templates, right: DH02 templates) are also shown.

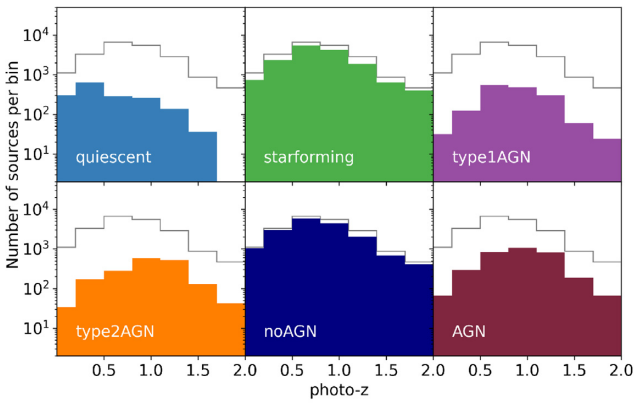

Figure 11. Redshift distributions for the four galaxy categories (coloured filled histograms) compared with the total distribution (open grey histogram). The two groups, no-AGN (quiescent and star-forming galaxies) and AGN (Type1 AGN and Type2 AGN), are also shown in the bottom-middle and bottom-right panels.

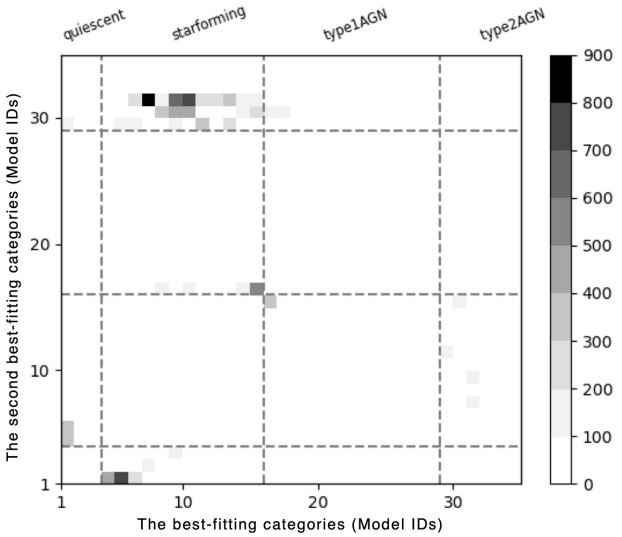

Figure 12. Density map of the best and second-best models. Only those models whose chi-square values are smaller than the critical value are shown. The boundaries between the categories are marked by the vertical and horizontal dashed lines.

categories, we have attempted to classify similar SEDs into the same category, but there are still cases where similar SEDs are included in different categories. We calculated the best chi-square values for each category and examined how many objects were below the threshold in several categories (Fig. 12). We find that many of the objects categorized as star-forming galaxies in the best fit are also successfully fitted by Type2-AGN SED models. However, not many of the best-fitting sources categorized as Type2 AGN are successfully fitted to the star-forming galaxies' SED model. This suggests that small contributing AGNs such as low-luminosity AGNs may be classified as star-forming galaxies. In Section 5.4, we construct a mean model for each category and perform SED fitting with them for the galaxy classification, which reduces the effect of multiple categories being equally well reproduced by the observed data.

Fig. 13 shows the distributions of $L_{\rm IR}$ of each category using SWIRE templates (left) or DH02 templates (right). The overall distributions are different when using the SWIRE and DH02 templates. The peak luminosity is roughly $L_{\rm IR} \sim 10^{12}\,{\rm L}_{\odot}$ in any category using either model, but the DH02 template tends to estimate the far-IR luminosity higher than the SWIRE template. We compared the chi-square values of both far-IR templates, and found that the SWIRE templates perform better in fitting the far-IR data compared to the DH02 templates. Specifically, the number of well-fitted sources (i.e. low chi-square values) by the DH02 template is only about 80 per cent compared to the SWIRE template. On the other hand, the number of less well-fitted objects (= higher chi-square values) is about 1.5 times larger than that of the SWIRE template. Specifically, the number of well-fitted sources (i.e. low chi-square values) by the SWIRE template is more than 1.2 times larger than that by the DH02 template. On the other hand, the number of less well-fitted objects (= high chi-squared values) is reduced to about 60 per cent. Furthermore, the number of objects that meet the chi-square's critical value using the SWIRE template (6827) is about 10 per cent larger than that using the DH02 template (6216). Hence, in the following discussion, we will use the results using the SWIRE template.

5.2 Evolution of SEDs

For each category, the photometric data points normalized by 5500 Å flux in each redshift bin against rest-frame wavelength are

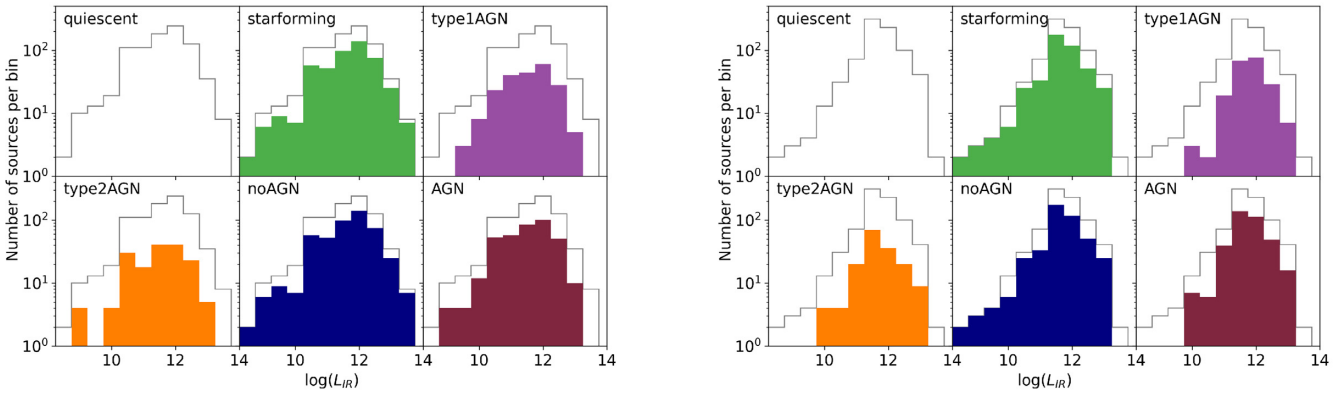

Figure 13. IR luminosity distributions using SWIRE far-IR model templates (left) and DH02 far-IR model templates (right) for the four galaxy categories (coloured filled histograms) compared with the total distribution (open grey histogram). The no-AGN and AGN groups are also shown in the bottom middle and right-hand panels.

plotted in Fig. 14. In this work, we divided the redshift range of 0.2–2.0 into four arbitrary redshift bins (z = 0.2–0.5, 0.5–1.0, 1.0–1.5, and 1.5–2.0). In addition, a 'typical SED' for each category, which has mean values of normalized photometric data in each 0.05 dex bin in the wavelength range of 0.1–1000 μm, and the model templates used for the categorization are also drawn. It seems that all the model templates in each category reproduce the observed data well in all the redshift bins. However, when we carefully look at the photometric data points for sources classified in the star-forming category, we find that the data points in the low-z (z = 0.2–0.5) bin show various flux densities at wavelengths of 3–10 μm spreading over the entire 12 model templates. However, in a high-redshift bin ($z > 1$), the data points are distributed only along the models showing high flux densities in that wavelength range.

Since these five models, which reproduce the observed data well at high redshifts, are the model templates originally classified as a starburst, it may suggest that most of star-forming galaxies in the high-z Universe contain a heat source capable of heating dust to temperatures that radiate thermal emission in the 3–10 μm range.

A possibility of the SED evolution of star-forming galaxies is reported by Curran & Duchesne (2018). They studied radio galaxies at $0.0021 < z < 5.19$ and found that rest-frame [3.4]–[4.6] and [4.6]–[12] of them are reddening with redshift. One possible source causing mid-IR excess is star clusters, but other possibility is low-luminosity or obscured AGNs. The template fitting approach used in this work does not allow us to determine the nature of this heat source. In a future study, we will perform SED fitting by constructing a galaxy model based on physical parameters. We have to mention here that the possibility of a bias that only bright objects are detected at high-z still remains.

In order to examine the effect, we selected the sources with $L_{IR} > 10^{12.5}$ $L_\odot$ and examined their SEDs in each redshift. At z = 0.2–0.5, the number of objects is too small to confirm the change. At z = 0.5–1.0, there is a slight increase of the mean flux in the 3–10 μm wavelength range, but it is not statistically significant (Fig. 15). This may indicate that the flux of star-forming galaxies in the middle IR is indeed increasing. In order to study this trend in detail, data covering a wide range of L_{IR} are needed.

5.3 Evolution of AGN fraction

In the local Universe, it is known that fraction of sources with AGN signatures increase with L_{IR} (Veilleux et al. 1995; Veilleux et al. 1999; Tran et al. 2001; Goto et al. 2011). Imanishi, Maiolino & Nakagawa (2010) showed that detectable buried AGN fraction in $z < 0.3$ at $L_{IR} = 10^{12.0–12.3}$ $L_\odot$ is ∼30 per cent and it increased up to ∼70 per cent at $L_{IR} = 10^{12.3–12.6}$ $L_\odot$. Kartaltepe et al. (2010) investigated 70 μm-selected galaxies in high-z Universe (<3.5 with a median redshift of 0.5) and found that the fraction increases from <5 per cent at $L_{IR} < 10^{11}$ $L_\odot$ to ∼100 per cent at $L_{IR} > 10^{13}$ $L_\odot$. With the large sample of our AKARI-HSC sample, we can investigate the fraction of sources with AGN signatures as a function of L_{IR} and also as a function of redshift. Since we investigate the AGN fraction depending on L_{IR}, we focus on sources for which L_{IR} could be measured in Section 5.1.

In this work, we considered galaxies for which the SEDs are reproduced by templates of Type1 AGN or Type2 AGN as AGN hosts. As mentioned in Section 4, the redshift accuracy of Type1 AGNs is not so high, we present the results for both cases, with and without Type1 AGNs. The AGN fraction is defined as a ratio of the number of AGN host to the total number of sources. We separated our objects with L_{IR} measurement into five L_{IR} bins, namely log L_{IR} = 11.0–11.5, 11.5–12.0, 12.0–12.5, 12.5–13.0, and 13.0–14.0, in each of the four redshift bins, and measured a fraction of AGN hosts in each redshift and L_{IR} bin. The values are summarized in Table 4 and plotted in Fig. 16.

The top left panel is the redshift evolution of the f_{AGN} when not including the Type1 AGNs. The figure shows that for all L_{IR} bins except the highest bin, the f_{AGN} tends to increase with increasing redshift. The f_{AGN} values of the objects included in the highest L_{IR} bin ($L_{IR} = 10^{13–14}$ $L_\odot$) do not show this increasing trend and are constant within the errors. This trend becomes stronger when the Type1 AGNs are included, as shown in the upper right panel. On the other hand, the change in f_{AGN} with L_{IR} is shown in the bottom panel. In the bottom left panel, which does not include the Type1 AGNs, we can see that the f_{AGN} tends to decrease with increasing L_{IR}. At z = 1.0–1.5, the only redshift bin covering the entire L_{IR} range shows a slight decrease or a roughly constant change. This trend can also be seen when we included the Type1 AGNs (bottom-right panel). These trends of f_{AGN} increasing with increasing redshift and decreasing with increasing L_{IR} are consistent with the results of Wang et al. (2020), which used a physically motivated SED model for an estimate of the ratio of the number of AGNs (= objects with a contribution of more than 20 per cent of AGN radiation to far-IR radiation) to the number of sources detected in the AKARI 18 μm band.

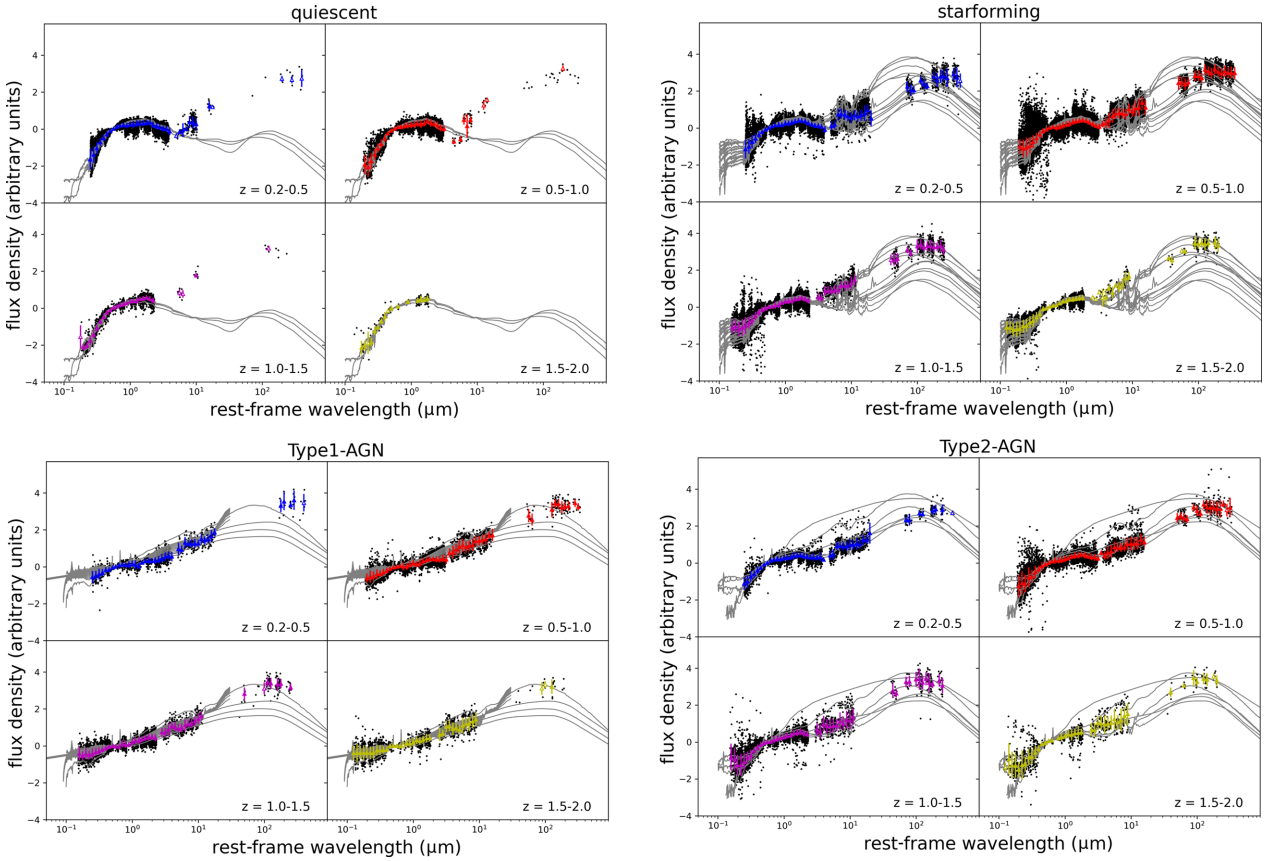

Figure 14. Rest-frame SEDs (black dots) normalized at 0.55 μm in each of the four redshift bins for each of the four galaxy categories. The redshift range is written in the bottom-right corner of each panel. The coloured triangles represent the mean values of the data in each 0.05 dex wavelength bin. The solid line is the SWIRE model template for each category.

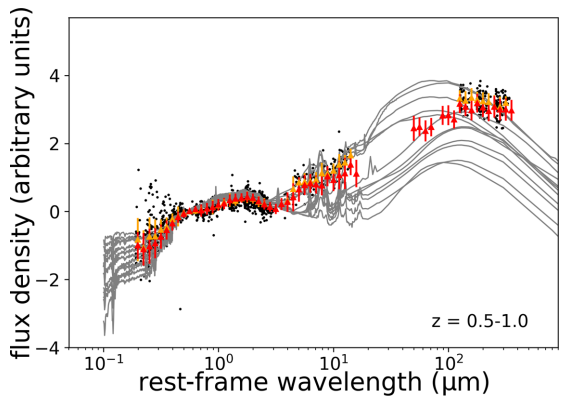

Figure 15. Comparison of the SEDs of star-forming galaxies with $L_{\rm IR} > 10^{12.5}\,{\rm L}_{\odot}$ and the SEDs of star-forming galaxies including all $L_{\rm IR}$. The black dots are photometric data points for star-forming galaxies with $L_{\rm IR} > 10^{12.5}\,{\rm L}_{\odot}$, and the orange triangles are the mean values. The red triangles are the same as those shown in the $z = 0.5 - 1.0$ panel in the top-right panel of Fig. 14 and are overlaid for comparison.

5.4 Examination of galaxy miscategorization

Fig. 16 shows that the $f_{\rm AGN}$ at low-z is ∼15 per cent , increasing to 20 per cent–30 per cent at $z \sim 1$, and to ∼40 per cent at $z \sim 2$. The value of $L_{\rm IR}$ at low-z in low-$L_{\rm IR}$ bin is consistent with the literature. Veilleux et al. (1999) found that the fraction of AGNs in the IRAS 1 Jy survey sample, which includes local galaxies ($<z>$ ∼0.2), is ∼15 per cent at $L_{\rm IR} = 10^{11.0–11.99}\,{\rm L}_{\odot}$, and ∼20 per cent at $L_{\rm IR} = 10^{12.0–12.29}\,{\rm L}_{\odot}$. Consistent with this, Rush et al. (1993) reported that the fraction of AGNs in the flux-limited IRAS Faint Source Catalog, Version 2 sample ($<z> = 0.009$) is ∼13 per cent. The fraction of AGN increases to about 25 per cent for sources with $L_{\rm IR} = 10^{11–12}\,{\rm L}_{\odot}$.

However, as seen in Fig. 16, the tendency for $f_{\rm AGN}$ to decrease with increasing $L_{\rm IR}$ at low-z is different from the results known from previous studies For example, Veilleux et al. (1999) reported that the $f_{\rm AGN}$ rapidly increases to ∼50 per cent at larger $L_{\rm IR}$ than $10^{12.3}\,{\rm L}_{\odot}$.

A possible explanation for this difference is the misclassification effect, which is caused by the similarity between the model template of star-forming galaxies and that of Type2 AGNs. As shown in the top-right panel of Fig. 14, the mid-IR flux of star-forming galaxies tends to increase at $z < 1$. Besides, as we see in Fig. 15, objects with larger $L_{\rm IR}$ tend to have larger mid-IR fluxes, even at $z < 1$. In other words, the SEDs of star-forming galaxies tend to be more similar to the SEDs of Type2 AGNs at high redshift and/or at high $L_{\rm IR}$, thereby increasing the probability of misclassification.

Hence, we construct a mean template for each category, taking the average of the templates belonging to each category, to avoid that similar shaped SEDs are in different categories (see Fig. 17). The mean SED model of the quiescent category has a shape with very weak ultraviolet (UV) emission from young stars and also weak far-IR thermal emission from dust. The mean model of the star-forming category has UV emission from young stars, a clear 1.6 μm bump, strong PAH emission features in the mid-IR, and thermal emission from dust in the far-IR. One of the Type1 AGNs has a flat SED from

Table 4. Summary of the number of AGNs and total galaxies in each L_{IR} bin and redshift bin. The numbers in the brackets include the Type1 AGNs. The bottom row is linear regression lines when an independent variable is an L_{IR} in each redshift bin, whereas the right column is linear regression lines when an independent variable is redshift in each L_{IR} bin. The coefficients of determination for each of the linear regression lines are written in a bracket.

		$z = 0.2$–0.5		$z = 0.5$–1.0		$z = 1.0$–1.5		$z = 1.5$–2.0		
The galaxy model	$\log(L_{IR}/L_\odot)$	AGN	Total	AGN	Total	AGN	Total	AGN	Total	Regression line (R^2)
SWIRE + Hybrid templates	11.0–11.5	73 (77)	414 (420)	167 (212)	488 (533)	12 (28)	29 (45)	0 (0)	0 (0)	$0.03z - 0.29(0.91)$ [$0.02z - 0.04(1.00)$]
	11.5–12.0	13 (19)	120 (126)	161 (224)	677 (740)	41 (86)	116 (161)	3 (3)	3 (3)	$0.04z - 0.07(0.99)$ [$0.02z + 0.02(1.00)$]
	12.0–12.5	1 (1)	29 (29)	50 (80)	293 (323)	59 (102)	226 (269)	4 (13)	8 (17)	$0.03z + 0.29(0.97)$ [$0.02z + 0.33(0.96)$]
	12.5–13.0	0 (0)	0 (0)	5 (13)	77 (85)	22 (39)	92 (109)	15 (30)	44 (59)	$0.04z + 0.49(0.98)$ [$0.03z + 0.30(0.99)$]
	13.0–14.0	0 (0)	0 (0)	1 (2)	2 (3)	6 (8)	20 (22)	4 (6)	15 (17)	– (–)
	Regression line (R^2)	$-0.07L + 12.51(1.00)$ [$-0.06L + 12.50(0.90)$]		$-0.06L + 13.13(0.99)$ [$-0.06L + 13.73(0.99)$]		$-0.09L + 15.02(0.50)$ [$-0.06L + 15.18(0.77)$]		$-0.05L + 14.68(0.90)$ [$-0.03L + 14.42(0.94)$]		
Mean templates	11.0–11.5	18 (26)	409 (417)	89 (139)	483 (533)	17 (36)	26 (45)	0 (0)	0 (0)	$1.37z + 0.38(0.94)$ [$0.01z + 0.35(0.96)$]
	11.5–12.0	7 (16)	117 (126)	169 (261)	648 (740)	64 (127)	98 (161)	2 (3)	2 (3)	$1.48z + 0.30(0.99)$ [$0.01z + 0.22(0.99)$]
	12.0–12.5	0 (0)	28 (28)	70 (120)	272 (322)	115 (203)	181 (269)	2 (15)	4 (17)	– [$0.02z + 0.04(0.92)$]
	12.5–13.0	0 (0)	0 (0)	24 (40)	69 (85)	47 (73)	84 (110)	23 (47)	35 (59)	$3.09z - 0.36(0.96)$ [$0.03z - 0.70(0.99)$]
	13.0–14.0	0 (0)	0 (0)	2 (3)	2 (3)	11 (13)	19 (21)	7 (14)	10 (17)	– (–)
	Regression line (R^2)	– –		$9.07L + 9.62(0.88)$ [$0.07L + 9.34(0.95)$]		$-16.91L + 22.72(0.73)$ [$-0.11L + 19.96(0.94)$]		– [$-0.08L + 19.79(0.34)$]		

the optical to mid-IR bands and thermal emission from the dust in the far-IR. One of the Type2 AGNs has a similar shape to star-forming galaxies in the optical but has a flat continuum emission in the mid-IR due to the hot dust heated by AGN. We used the same setting for the LE PHARE code as the one in Section 5.1. The far-IR model also uses the same SWIRE templates. The classification of galaxies was performed in the same manner as before, based on the categories of SED templates that were able to reproduce the SED of an object with a minimum chi-square. The SED fitting with a small variety of templates decreases the number of objects that can be fitted below the chi-square's critical value, yet it can lessen the misclassification of objects that are difficult to determine whether they are star-forming galaxies or Type2 AGNs.

The redshift and L_{IR} dependence of the f_{AGN} using this result are plotted in Fig. 18. The tendency for f_{AGN} to increase with increasing redshift is more pronounced than that seen in Fig. 16, due to a decrease in misclassification at high redshifts. On the other hand, the decreasing tendency of f_{AGN} with increasing L_{IR} became moderately increasing at low-z and almost constant at high-z due to a decrease in misclassification at high L_{IR}.

Kartaltepe et al. (2010) found that the fraction of AGNs in the 70 μm-detected samples (redshift range is $z = 0.01$–3.5 with a median redshift of 0.5) strongly increases with increasing L_{IR} and reached ∼80 per cent at $L_{IR} \sim 10^{13}\,L_\odot$. However, we could not find a strong increase in f_{AGN} with increasing L_{IR}. The difference between these results can be explained by whether the samples were divided into redshift bins or not. Kartaltepe et al. (2010) divided their samples into eight L_{IR} bins but not dividing them into any redshift bins. In contrast, we divided our sample into redshift bins as well and calculated f_{AGN}. When we sum the number of AGN and no-AGN sources in the entire redshift range and calculate f_{AGN} in each L_{IR} bin, the f_{AGN} is 13.5 per cent, 28.0 per cent, 38.6 per cent, 50.0 per cent, and 64.5 per cent from the smallest L_{IR} bin. This shows that f_{AGN} seems to increase with increasing L_{IR}.

Chiang et al. (2019) also investigated the AGN fraction using our AKARI-HSC sample, and found an AGN fraction dependence on L_{IR} but not on z. Their result seems to be inconsistent with our results. Chiang et al. (2019) used SWIRE model templates as 'far-IR templates' to fit data at larger than 7 μm, and distinguished AGNs from no-AGN galaxies according to the galaxy type given in Polletta et al. (2007). On the other hand, we used the same SWIRE model templates but as 'galaxy templates' to fit all the data from optical to far-IR wavelength, and distinguish AGNs. We are afraid that the AGN distinction using mid-IR to far-IR data (i.e. >7 μm) in Polletta et al. (2007) accounts for the inconsistency.

In order to show the tendency we have seen from Fig. 16 statistically, we performed regression analysis. This time, we simply studied whether the AGN fraction and L_{IR} or z are in a positive linear correlation. Regression lines and coefficient of determinations are summarized in the rightmost column (AGN fraction versus z) and bottom row (AGN fraction versus L_{IR}) of Table 4. This regression analysis clearly shows that the AGN fraction and z are strongly correlated in any L_{IR} range. On the other hand, we can see a sign of the positive correlation between the AGN fraction and L_{IR} at $z < 1$, but no positive correlations are seen at higher redshift.

As shown in Section 4, the photo-z accuracy of our AKARI-HSC sample is ∼0.06, which means that photo-z at $z \sim 1$ may be wrong by about 0.1 from the correct redshift. We tested the effect of these photo-z uncertainties on the f_{AGN} distribution. We shifted the redshift bin by 0.1 and estimated the f_{AGN} distribution in each redshift bin of $z = 0.3$–0.6, 0.6–1.1, 1.1–1.6, and 1.6–2.1. At this time, we used the same L_{IR} bins as before. As can be seen in Fig. 18, the strong positive correlation between f_{AGN} and redshift and the tendency for the value to remain unchanged regardless of the L_{IR} are still evident, even when the redshift bins are shifted. This implies that the effect of the photo-z uncertainty is insignificant.

We mention here that our AKARI-HSC sample is a flux-limited and area-limited sample, so little to none low-luminosity galaxies are

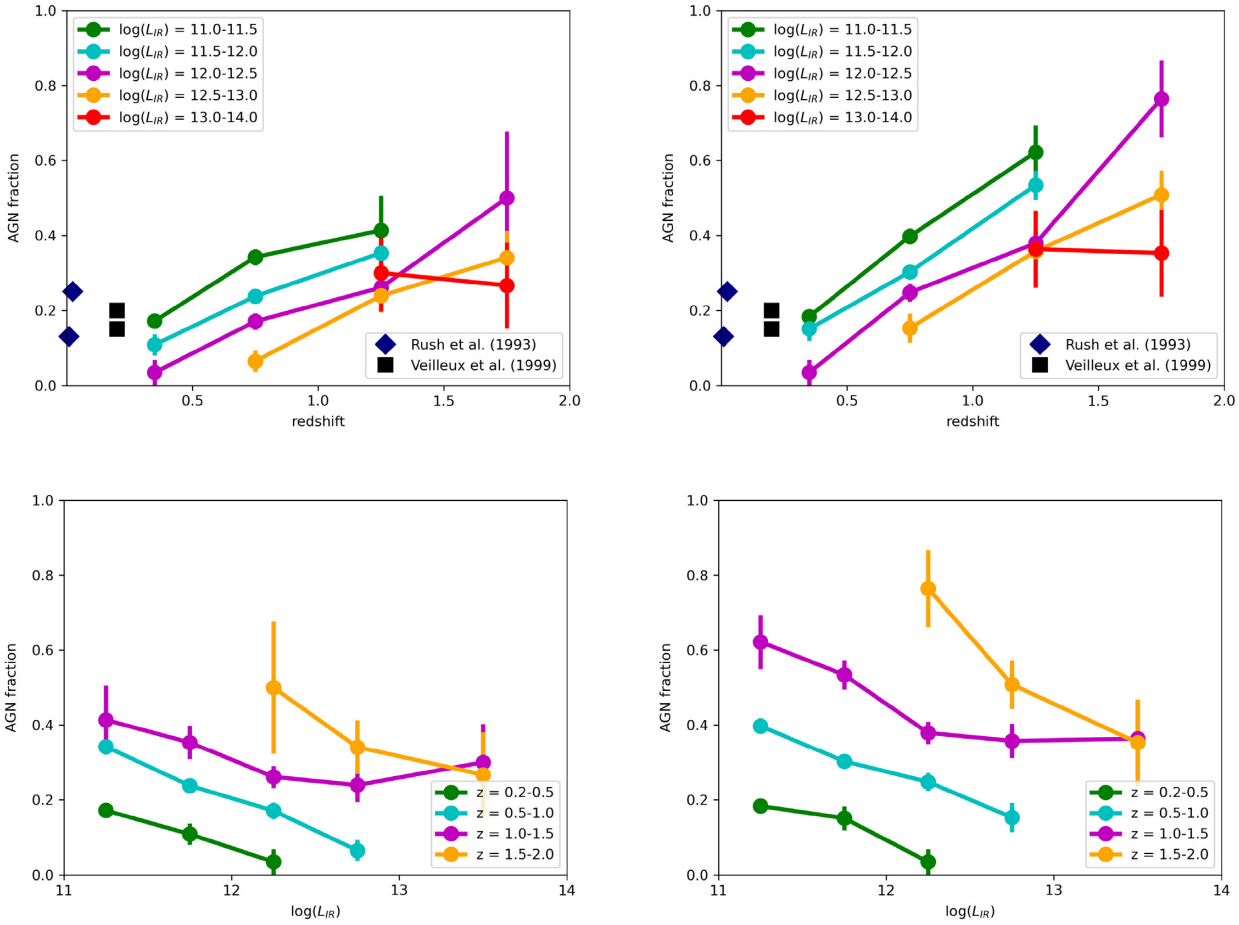

Figure 16. The fraction of AGN against redshift in each $L_{\rm IR}$ bin (top panels) and $L_{\rm IR}$ in each redshift bin (bottom panels). 1σ of the binomial distribution error bars are shown. Type1 AGNs are not included in the left-hand side panels and included in the right-hand side panels. Data points in bins that contain less than five galaxies are excluded from this figure for clarity. The squares and the diamonds represent the literature results (Rush, Malkan & Spinoglio 1993; Veilleux, Kim & Sanders 1999).

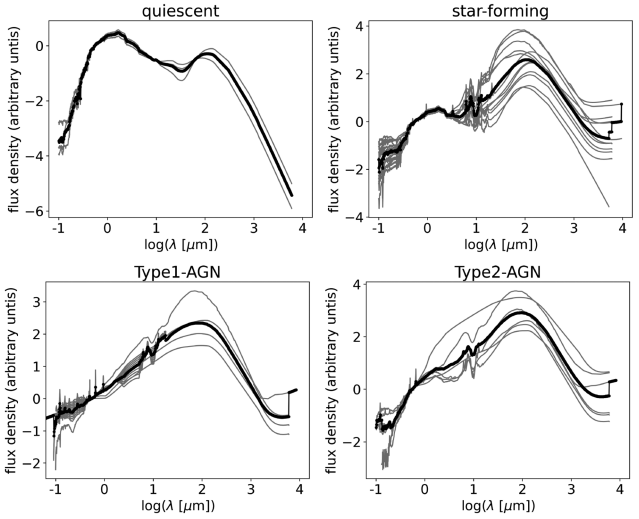

Figure 17. Mean templates of each category, namely quiescent, star forming, Type1 AGN, and Type2 AGN, are from the top left panel to the bottom-right panel. SED templates written with grey lines are ones written in Fig. 9, and the black thick lines are the mean of these SED templates in each category.

detected at high-redshift ranges and little to none high-luminosity galaxies are detected at low-redshift ranges. We examined these effects. Goto et al. (2019) estimated that the 8 μm luminosity ($\nu L_{\nu,\,8\,\mu\rm m}$) corresponding to the flux limit in the AKARI filters is $\log(\nu L_{\nu,\,8\,\mu\rm m}/\rm L_\odot) = \sim$9.70, $\sim$10.65, $\sim$10.80, and $\sim$11.70 at $z =$ 0.38, 0.78, 1.25, and 2.00, respectively. These $\nu L_{\nu,\,8\,\mu\rm m}$ values are corresponding to $\log(L_{\rm TIR}/\rm L_\odot) = \sim$10.4, $\sim$11.3, $\sim$11.5, and $\sim$12.3 using the relation $L_{\rm TIR}(\rm L_\odot) = (20 \pm 5) \times \nu L_{\nu,8\,\mu\rm m}^{0.94\pm0.01}$ obtained using the galaxy sample from the AKARI Far-Infrared All-Sky Survey (Goto et al. 2011). At each redshift, some sources fainter than this limiting luminosity may fail to be detected. Specifically, the results for $\log(L_{\rm IR}/\rm L_\odot) = 11.0$–$11.5$ at $z > 0.5$ and $\log(L_{\rm IR}/\rm L_\odot) > 12$ at $z =$ 1.5–2.0 may be affected by this missing detection, yet the majority of our results are unaffected. In contrast, our AKARI-HSC sample is an area-limited sample and the low-z results may be affected by this. Symeonidis & Page (2019) showed that the number densities of LIRGs hosting AGNs at $\log(L_{\rm IR}/\rm L_\odot) = 11.5$ and ULIRGs hosting AGNs at $\log(L_{\rm IR}/\rm L_\odot) = 12.0$ are $\phi_{11.5}$ ($\rm Mpc^{-3}\ log\mathit{L}^{-1}$) $\sim 10^{-6.25}$ and $\phi_{12.0} \sim 10^{-6.85}$, respectively, at $z = 0.186$. These values correspond to densities that 1.3 LIRGs hosting AGNs and 0.33 ULIRGs hosting AGNs are expected to be found in the 5.4 square deg NEP-Wide survey area at $z \sim 0.2$. This probably accounts for the smaller density than previous studies of $f_{\rm AGN}$ at $z =$ 12.0–12.5 in Fig. 16.

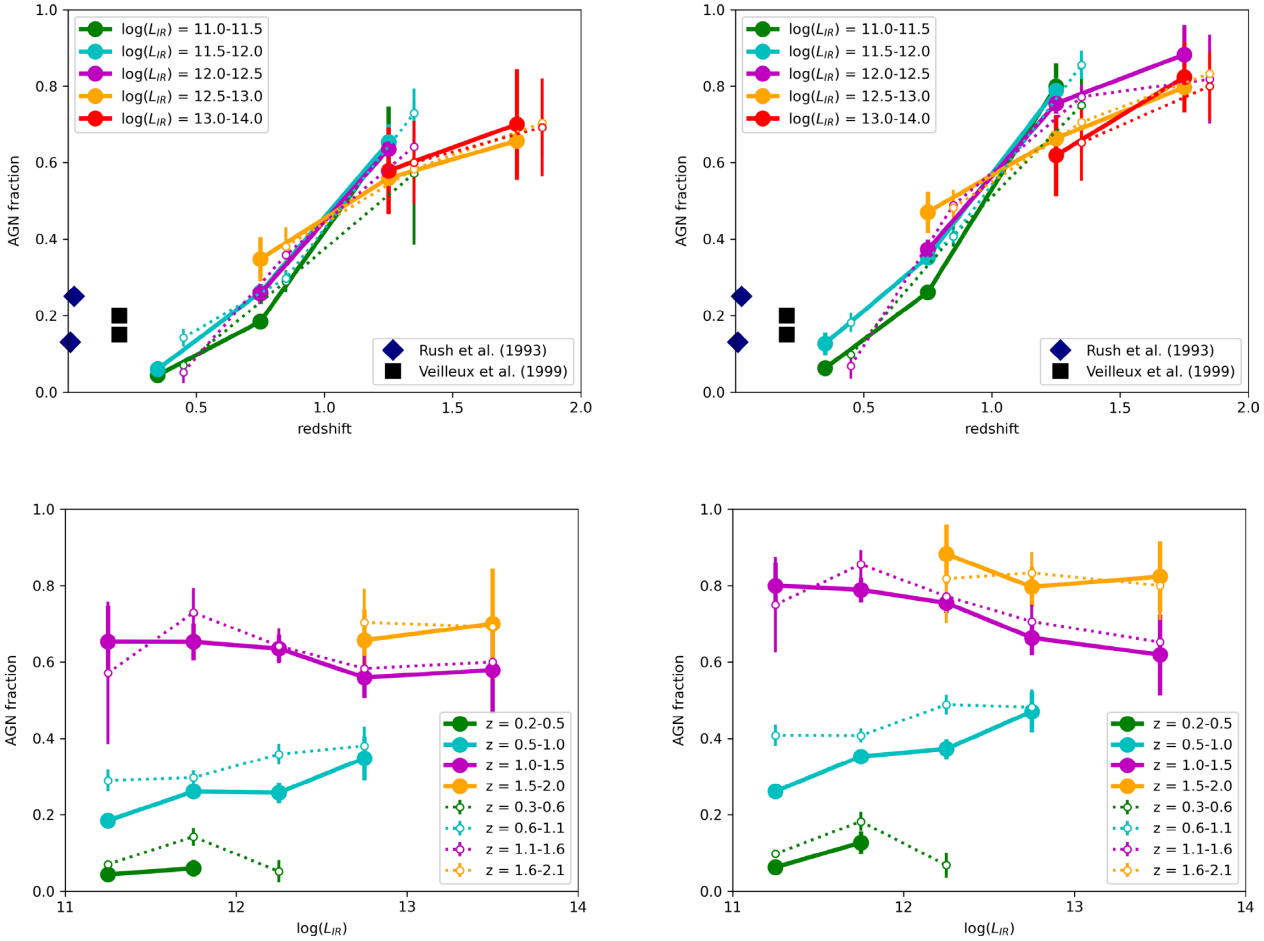

Figure 18. The same as Fig. 16, but using the mean SED templates. The open circles with dotted lines indicate the results when the redshift bin is shifted by 0.1.

6 SUMMARY

We have obtained *g*-, *r*-, *i*-, *z*-, and *y*-band images with Subaru/HSC covering the 5.4 sq. deg AKARI NEP-Wide field. The 5σ detection limits are 28.1, 26.8, 26.3, 25.5, and 25.0 mag in the *g*, *r*, *i*, *z*, and *y* bands, respectively. From the deep HSC optical data, we extracted more than 2.6 million sources with valid photometric data. We carried out cross-matches between the HSC and AKARI NEP-Wide catalogues to produce a band-merged catalogue. The catalogues contain 70 959 entries. We cross-identified with existing multiband data from optical u^* to far-IR wavelengths to build up SEDs of IR galaxies detected by AKARI and HSC. We achieved photometric redshifts using the SEDs with template fitting with an accuracy of $\sigma_{\Delta z/(1+zs)} \sim 0.06$ and an outlier rate of ∼13.4 per cent at $0.2 < z < 1.5$.

We conducted SED fitting with empirical SED models of local galaxies to classify the IR galaxies into four categories, namely quiescent, star forming, Type1 AGN, and Type2 AGN, in four redshift bins of $z = 0.2$–0.5, 0.5–1.0, 1.0–1.5, and 1.5–2.0. We found that the mean mid-IR flux of star-forming galaxies at $z > 1$ tends to be much larger than what can be explained by SED models of spiral galaxies in the local Universe. This indicates that the majority of high-*z* star-forming galaxies have energy sources (e.g. star clusters, low-luminosity AGNs, or obscured AGNs) that can heat the dust to high temperatures.

Finally, we divided the IR luminosity range of $\log(L_{\rm IR}/{\rm L}_\odot) = 11.0$–14.0 into five bins and studied the *z* dependence and $L_{\rm IR}$ dependence of the fraction of AGNs in the IR galaxies. We found that the AGN fraction increases with increasing redshift in all $L_{\rm IR}$ bins. This can be seen more prominently in the classification result using the mean models to lessen the effect of misclassification due to the similarity of model templates between different categories. On the other hand, the $L_{\rm IR}$ dependence of $f_{\rm AGN}$ showed a modest increase at low-*z* ($z < 1$) and a flat trend at high-*z* ($z > 1$), when the effect of misclassification was minimized.

The multiband catalogue we constructed and calculated photo-*z* for the AKARI NEP-Wide IR galaxies encourages a statistical investigation such as the evolution of the IR galaxy properties, their contribution to the star formation history, and/or the relationship between AGN and star formation activity.

ACKNOWLEDGEMENTS

We would like to express our deepest gratitude to the referee for his/her profound insights, observations, useful comments, and suggestions. We thank P. Paul for creating astrometric catalogue from the Pan-STARRS1 Surveys (PS1) data. This work is supported by the Japan Society for the Promotion of Science (JSPS; grant number 23244040). T. Goto acknowledges the support by the Ministry of Science and Technology of Taiwan (MOST) through grants 105-2112-M-007-003-MY3 and 108-2628-M-007-004-MY3, and Y. Ohyama acknowledges the support by the MOST through grant 107-2119-M-001-026. The PS1 have been made possible through contributions

of the Institute for Astronomy, the University of Hawaii, the Pan-STARRS Project Office, the Max-Planck Society and its participating institutes, the Max Planck Institute for Astronomy, Heidelberg and the Max Planck Institute for Extraterrestrial Physics, Garching, The Johns Hopkins University, Durham University, the University of Edinburgh, Queen's University Belfast, the Harvard-Smithsonian Center for Astrophysics, the Las Cumbres Observatory Global Telescope Network Incorporated, the National Central University of Taiwan, the Space Telescope Science Institute, the National Aeronautics and Space Administration under Grant No. NNX08AR22G issued through the Planetary Science Division of the NASA Science Mission Directorate, the National Science Foundation under Grant No. AST-1238877, the University of Maryland, and Eotvos Lorand University (ELTE). This publication makes use of data products from the Wide-field Infrared Survey Explorer, which is a joint project of the University of California, Los Angeles, and the Jet Propulsion Laboratory/California Institute of Technology, and *NEOWISE*, which is a project of the Jet Propulsion Laboratory/California Institute of Technology. *WISE* and *NEOWISE* are funded by the National Aeronautics and Space Administration. We are grateful for the support of HSC help desk. We would like to express our acknowledgement to the indigenous Hawaiian people for their understanding of the significant role of the summit of Maunakea in astronomical research.

DATA AVAILABILITY

The data underlying this article will be shared on reasonable request to the corresponding author.

REFERENCES

Aihara H. et al., 2018, PASJ, 70, S8
Arnouts S. et al., 2007, A&A, 476, 137
Bertin E., Arnouts S., 1996, A&AS, 117, 393
Bohlin R. C., Colina L., Finley D. S., 1995, AJ, 110, 1316
Bosch J. et al., 2018, PASJ, 70, S5
Buat V. et al., 2015, A&A, 577, A141
Burgarella D. et al., 2019, PASJ, 71, 12
Calzetti D., Armus L., Bohlin R. C., Kinney A. L., Koornneef J., Storchi-Bergmann T., 2000, ApJ, 533, 682
Caputi K. I. et al., 2007, ApJ, 660, 97
Cardelli J. A., Clayton G. C., Mathis J. S., 1989, ApJ, 345, 245
Chambers K. C. et al., 2016, preprint (arXiv:1612.05560)
Chiang C.-Y., Goto T., Hashimoto T., Kim S. J., Matsuhara H., Oi N., 2019, PASJ, 71, 31
Coleman G. D., Wu C. C., Weedman D. W., 1980, ApJS, 43, 393
Curran S. J., Duchesne S. W., 2018, MNRAS, 476, 3580
Cutri R. M. et al., 2013, VizieR Online Data Catalogue, II/328, https://ui.adsabs.harvard.edu/abs/2013wise.rept....1C
Dale D. A., Helou G., 2002, ApJ, 576, 159
Elston R. J. et al., 2006, ApJ, 639, 816
Fazio G. G. et al., 2004, ApJS, 154, 10
Franceschini A., Rodighiero G., Vaccari M., 2008, A&A, 487, 837
Geach J. E. et al., 2017, MNRAS, 465, 1789
Goto T. et al., 2010, A&A, 514, A6
Goto T. et al., 2011, MNRAS, 410, 573
Goto T. et al., 2015, MNRAS, 452, 1684
Goto T. et al., 2019, PASJ, 71, 30
Hanami H. et al., 2012, PASJ, 64, 70
Hoaglin D. C., Mosteller F., Tukey J. W., 1983, Understanding Robust and Exploratory Data Analysis, Wiley
Houck J. R. et al., 2004, ApJS, 154, 18
Huang T.-C., Goto T., Hashimoto T., Oi N., Matsuhara H., 2017, MNRAS, 471, 4239
Huang S. et al., 2018, PASJ, 70, S6
Huang T.-C. et al., 2020, MNRAS, 498, 609
Hudelot P., et al., 2012, VizieR Online Data Catalog, II/317, https://www.cfht.hawaii.edu/Science/CFHLS/T0007/
Hwang N. et al., 2007, ApJS, 172, 583
Ilbert O. et al., 2006, A&A, 457, 841
Ilbert O. et al., 2009, ApJ, 690, 1236
Imanishi M., Maiolino R., Nakagawa T., 2010, ApJ, 709, 801
Jeon Y., Im M., Ibrahimov M., Lee H. M., Lee I., Lee M. G., 2010, ApJS, 190, 166
Jeon Y., Im M., Kang E., Lee H. M., Matsuhara H., 2014, ApJS, 214, 20
Karouzos M. et al., 2014, ApJ, 784, 137
Kartaltepe J. S. et al., 2010, ApJ, 709, 572
Kim D. C., Veilleux S., Sanders D. B., 1998, ApJ, 508, 627
Kim S. J. et al., 2012, A&A, 548, A29
Kim S. J. et al., 2015, MNRAS, 454, 1573
Kim H. K., Malkan M. A., Oi N., Burgarella D., Buat V., Takagi T., Matsuhara H., 2018, in Ootsubo T., Yamamura I., Murata K., Onaka T., eds, The Cosmic Wheel and the Legacy of the AKARI Archive: From Galaxies and Stars to Planets and Life. Japan Aerospace Exploration Agency (JAXA), p. 371
Kim S. J. et al., 2019, PASJ, 71, 11
Kim S. J. et al., 2020, MNRAS, in press
Kinney A. L., Calzetti D., Bohlin R. C., McQuade K., Storchi-Bergmann T., Schmitt H. R., 1996, ApJ, 467, 38
Kron R. G., 1980, ApJS, 43, 305
Krumpe M. et al., 2015, MNRAS, 446, 911
Lagache G., Abergel A., Boulanger F., Désert F. X., Puget J. L., 1999, A&A, 344, 322
Le Floc'h E. et al., 2005, ApJ, 632, 169
Lee H. M. et al., 2009, PASJ, 61, 375
Magnier E. A. et al., 2013, ApJS, 205, 20
Matsuhara H. et al., 2006, PASJ, 58, 673
Miyazaki S. et al., 2012, in Ian S. M., Suzanne K. R., Hideki T., eds, Proc. SPIE Conf. Ser. Vol. 8446, Ground-Based and Airborne Instrumentation for Astronomy IV. SPIE, Bellingham, p. 84460Z
Miyazaki S. et al., 2018, PASJ, 70, S1
Murakami H. et al., 2007, PASJ, 59, S369
Murata K. et al., 2013, A&A, 559, A132
Murata K. et al., 2014, A&A, 566, A136
Murphy T. W. J., Armus L., Matthews K., Soifer B. T., Mazzarella J. M., Shupe D. L., Strauss M. A., Neugebauer G., 1996, AJ, 111, 1025
Nayyeri H. et al., 2018, ApJS, 234, 38
Nguyen H. T. et al., 2010, A&A, 518, L5
Oi N. et al., 2014, A&A, 566, A60
Oi N., Goto T., Malkan M., Pearson C., Matsuhara H., 2017, PASJ, 69, 70
Onaka T. et al., 2007, PASJ, 59, S401
Pearson C. P. et al., 2014, MNRAS, 444, 846
Pearson C. et al., 2017, Publ. Korean Astron. Soc., 32, 219
Pearson C. et al., 2019, PASJ, 71, 13
Pickles A. J., 1998, PASP, 110, 863
Polletta M. et al., 2007, ApJ, 663, 81
Puget J. L., Abergel A., Bernard J. P., Boulanger F., Burton W. B., Desert F. X., Hartmann D., 1996, A&A, 308, L5
Rieke G. H. et al., 2004, ApJS, 154, 25
Rush B., Malkan M. A., Spinoglio L., 1993, ApJS, 89, 1
Salvato M. et al., 2009, ApJ, 690, 1250
Sanders D. B., Mirabel I. F., 1996, ARA&A, 34, 749
Schlafly E. F. et al., 2012, ApJ, 756, 158
Schlegel D. J., Finkbeiner D. P., Davis M., 1998, ApJ, 500, 525
Shim H. et al., 2013, ApJS, 207, 37
Shogaki A. et al., 2018, in Ootsubo T., Yamamura I., Murata K., Onaka T., eds, The Cosmic Wheel and the Legacy of the AKARI Archive: From Galaxies and Stars to Planets and Life. Japan Aerospace Exploration Agency (JAXA), p. 367
Stecker F. W., Malkan M. A., Scully S. T., 2006, ApJ, 648, 774
Symeonidis M., Page M. J., 2019, MNRAS, 485, L11

Takagi T. et al., 2012, A&A, 537, A24
Tanaka M. et al., 2018, PASJ, 70, S9
Toba Y. et al., 2020, ApJ, 899, 35
Tonry J. L. et al., 2012, ApJ, 750, 99
Tran Q. D. et al., 2001, ApJ, 552, 527
Veilleux S., Kim D. C., Sanders D. B., Mazzarella J. M., Soifer B. T., 1995, ApJS, 98, 171
Veilleux S., Kim D. C., Sanders D. B., 1999, ApJ, 522, 113
Wada T. et al., 2008, PASJ, 60, S517
Wang T.-W. et al., 2020, MNRAS, 499, 4068
White G. J. et al., 2010, A&A, 517, A54

This paper has been typeset from a TEX/LATEX file prepared by the author.